Title

Cross-correlation of Dark Energy Survey Year 3 lensing data with ACT and Planck thermal Sunyaev-Zel'dovich effect observations. I. Measurements, systematics tests, and feedback model constraints

Authors

Gatti, M
Pandey, S
Baxter, E
et al.

Cross-correlation of DES Y3 lensing and ACT/*Planck* thermal Sunyaev Zel'dovich Effect I: Measurements, systematics tests, and feedback model constraints

M. Gatti,[1, *] S. Pandey,[1] E. Baxter,[2] J. C. Hill,[3, 4] E. Moser,[5] M. Raveri,[1] X. Fang,[6] J. DeRose,[7] G. Giannini,[8] C. Doux,[1]
H. Huang,[9] N. Battaglia,[5] A. Alarcon,[10] A. Amon,[11] M. Becker,[10] A. Campos,[12] C. Chang,[13, 14] R. Chen,[15] A. Choi,[16]
K. Eckert,[1] J. Elvin-Poole,[16, 17] S. Everett,[18] A. Ferte,[19] I. Harrison,[20, 21] N. Maccrann,[22] J. Mccullough,[11] J. Myles,[23, 11, 24]
A. Navarro Alsina,[25] J. Prat,[13, 14] R.P. Rollins,[21] C. Sanchez,[1] T. Shin,[1] M. Troxel,[15] I. Tutusaus,[26, 27] B. Yin,[12] T. Abbott,[28]
M. Aguena,[29] S. Allam,[30] F. Andrade-Oliveira,[31, 29] J. Annis,[30] G. Bernstein,[1] E. Bertin,[32, 33] B. Bolliet,[34] J. R. Bond,[35]
D. Brooks,[36, 11, 24] D. L. Burke,[11, 24] E. Calabrese,[37] A. Carnero Rosell,[38, 29, 39] M. Carrasco Kind,[40, 41] J. Carretero,[8]
R. Cawthon,[42] M. Costanzi,[43, 44, 45] L. N. da Costa,[29, 46] M. Crocce,[26, 27] L. N. da Costa,[29, 46] M. E. da Silva Pereira,[47] J. De Vicente,[48]
S. Desai,[49] H. T. Diehl,[30] J. P. Dietrich,[50] P. Doel,[36] J. Dunkley,[51, 52] A. E. Evrard,[53, 47] S. Ferraro,[54, 55] I. Ferrero,[56]
B. Flaugher,[30] P. Fosalba,[26, 27] J. Frieman,[30, 14] J. García-Bellido,[57] E. Gaztanaga,[26, 27] D. W. Gerdes,[53, 47] T. Giannantonio,[58, 59]
D. Gruen,[50] R. A. Gruendl,[40, 41] J. Gschwend,[29, 46] G. Gutierrez,[30] K. Herner,[30] A. D. Hincks,[60] S. R. Hinton,[61]
D. L. Hollowood,[18] K. Honscheid,[16, 17] J. P. Hughes,[62] D. Huterer,[47] B. Jain,[1] D. J. James,[63] E. Krause,[6] K. Kuehn,[64, 65]
N. Kuropatkin,[30] O. Lahav,[36] C. Lidman,[66, 67] M. Lima,[68, 29] M. Lokken,[60, 35, 69] M. S. Madhavacheril,[70] M. A. G. Maia,[29, 46]
J. L. Marshall,[71] J.J. Mcmahon,[72, 73, 74, 75] P. Melchior,[51] K. Moodley,[76, 77] J. J. Mohr,[50, 78] R. Morgan,[42] F. Nati,[79]
M. D. Niemack,[5, 5, 80] L. Page,[52] A. Palmese,[30, 14] F. Paz-Chinchón,[40, 58] A. Pieres,[29, 46] A. A. Plazas Malagón,[51]
M. Rodriguez-Monroy,[48] A. K. Romer,[81] E. Sanchez,[48] V. Scarpine,[30] E. Schaan,[54, 55] L. F. Secco,[1, 14] S. Serrano,[26, 27]
E. Sheldon,[82] B. D. Sherwin,[83, 59] C. Sifón,[84] M. Smith,[85] M. Soares-Santos,[47] D. Spergel,[86, 87] E. Suchyta,[88] G. Tarle,[47]
D. Thomas,[89] C. To,[23, 11, 24] D. L. Tucker,[30] T. N. Varga,[78, 90] J. Weller,[78, 90] R.D. Wilkinson,[81] E. J. Wollack,[91] and Z. Xu[92, 1]

(DES and ACT Collaboration)

[1]*Department of Physics and Astronomy, University of Pennsylvania, Philadelphia, PA 19104, USA*
[2]*Institute for Astronomy, University of Hawai'i, 2680 Woodlawn Drive, Honolulu, HI 96822, USA*
[3]*Department of Physics, Columbia University, New York, NY, USA 10027*
[4]*Center for Computational Astrophysics, Flatiron Institute, New York, NY, USA 10010*
[5]*Department of Astronomy, Cornell University, Ithaca, NY 14853, USA*
[6]*Department of Astronomy/Steward Observatory, University of Arizona,*
933 North Cherry Avenue, Tucson, AZ 85721-0065, USA
[7]*Lawrence Berkeley National Laboratory, 1 Cyclotron Road, Berkeley, CA 94720, USA*
[8]*Institut de Física d'Altes Energies (IFAE), The Barcelona Institute of*
Science and Technology, Campus UAB, 08193 Bellaterra (Barcelona) Spain
[9]*Department of Physics, University of Arizona, Tucson, AZ 85721, USA*
[10]*Argonne National Laboratory, 9700 South Cass Avenue, Lemont, IL 60439, USA*
[11]*Kavli Institute for Particle Astrophysics & Cosmology,*
P. O. Box 2450, Stanford University, Stanford, CA 94305, USA
[12]*Department of Physics, Carnegie Mellon University, Pittsburgh, Pennsylvania 15312, USA*
[13]*Department of Astronomy and Astrophysics, University of Chicago, Chicago, IL 60637, USA*
[14]*Kavli Institute for Cosmological Physics, University of Chicago, Chicago, IL 60637, USA*
[15]*Department of Physics, Duke University Durham, NC 27708, USA*
[16]*Center for Cosmology and Astro-Particle Physics, The Ohio State University, Columbus, OH 43210, USA*
[17]*Department of Physics, The Ohio State University, Columbus, OH 43210, USA*
[18]*Santa Cruz Institute for Particle Physics, Santa Cruz, CA 95064, USA*
[19]*Jet Propulsion Laboratory, California Institute of Technology, 4800 Oak Grove Dr., Pasadena, CA 91109, USA*
[20]*Department of Physics, University of Oxford, Denys Wilkinson Building, Keble Road, Oxford OX1 3RH, UK*
[21]*Jodrell Bank Center for Astrophysics, School of Physics and Astronomy,*
University of Manchester, Oxford Road, Manchester, M13 9PL, UK
[22]*Department of Applied Mathematics and Theoretical Physics, University of Cambridge, Cambridge CB3 0WA, UK*
[23]*Department of Physics, Stanford University, 382 Via Pueblo Mall, Stanford, CA 94305, USA*
[24]*SLAC National Accelerator Laboratory, Menlo Park, CA 94025, USA*
[25]*Instituto de Física Gleb Wataghin, Universidade Estadual de Campinas, 13083-859, Campinas, SP, Brazil*
[26]*Institut d'Estudis Espacials de Catalunya (IEEC), 08034 Barcelona, Spain*
[27]*Institute of Space Sciences (ICE, CSIC), Campus UAB,*
Carrer de Can Magrans, s/n, 08193 Barcelona, Spain
[28]*Cerro Tololo Inter-American Observatory, NSF's National Optical-Infrared Astronomy Research Laboratory, Casilla 603, La Serena, Chile*
[29]*Laboratório Interinstitucional de e-Astronomia - LIneA,*
Rua Gal. José Cristino 77, Rio de Janeiro, RJ - 20921-400, Brazil
[30]*Fermi National Accelerator Laboratory, P. O. Box 500, Batavia, IL 60510, USA*
[31]*Instituto de Física Teórica, Universidade Estadual Paulista, São Paulo, Brazil*
[32]*CNRS, UMR 7095, Institut d'Astrophysique de Paris, F-75014, Paris, France*
[33]*Sorbonne Universités, UPMC Univ Paris 06, UMR 7095,*
Institut d'Astrophysique de Paris, F-75014, Paris, France

[34]*Department of Physics, Columbia University, New York, NY 10027, USA*

[35]*Canadian Institute for Theoretical Astrophysics, 60 St. George Street,*
University of Toronto, Toronto, ON, M5S 3H8, Canada

[36]*Department of Physics & Astronomy, University College London, Gower Street, London, WC1E 6BT, UK*

[37]*School of Physics and Astronomy, Cardiff University, The Parade, Cardiff, CF24 3AA, UK*

[38]*Instituto de Astrofisica de Canarias, E-38205 La Laguna, Tenerife, Spain*

[39]*Universidad de La Laguna, Dpto. Astrofísica, E-38206 La Laguna, Tenerife, Spain*

[40]*Center for Astrophysical Surveys, National Center for Supercomputing Applications, 1205 West Clark St., Urbana, IL 61801, USA*

[41]*Department of Astronomy, University of Illinois at Urbana-Champaign, 1002 W. Green Street, Urbana, IL 61801, USA*

[42]*Physics Department, 2320 Chamberlin Hall, University of Wisconsin-Madison, 1150 University Avenue Madison, WI 53706-1390*

[43]*Astronomy Unit, Department of Physics, University of Trieste, via Tiepolo 11, I-34131 Trieste, Italy*

[44]*INAF-Osservatorio Astronomico di Trieste, via G. B. Tiepolo 11, I-34143 Trieste, Italy*

[45]*Institute for Fundamental Physics of the Universe, Via Beirut 2, 34014 Trieste, Italy*

[46]*Observatório Nacional, Rua Gal. José Cristino 77, Rio de Janeiro, RJ - 20921-400, Brazil*

[47]*Department of Physics, University of Michigan, Ann Arbor, MI 48109, USA*

[48]*Centro de Investigaciones Energéticas, Medioambientales y Tecnológicas (CIEMAT), Madrid, Spain*

[49]*Department of Physics, IIT Hyderabad, Kandi, Telangana 502285, India*

[50]*Faculty of Physics, Ludwig-Maximilians-Universität, Scheinerstr. 1, 81679 Munich, Germany*

[51]*Department of Astrophysical Sciences, Princeton University, Peyton Hall, Princeton, NJ 08544, USA*

[52]*Department of Physics, Jadwin Hall, Princeton University, Princeton, NJ 08544-0708, USA*

[53]*Department of Astronomy, University of Michigan, Ann Arbor, MI 48109, USA*

[54]*Lawrence Berkeley National Laboratory, One Cyclotron Road, Berkeley, CA 94720, USA*

[55]*Berkeley Center for Cosmological Physics, UC Berkeley, CA 94720, USA*

[56]*Institute of Theoretical Astrophysics, University of Oslo. P.O. Box 1029 Blindern, NO-0315 Oslo, Norway*

[57]*Instituto de Fisica Teorica UAM/CSIC, Universidad Autonoma de Madrid, 28049 Madrid, Spain*

[58]*Institute of Astronomy, University of Cambridge, Madingley Road, Cambridge CB3 0HA, UK*

[59]*Kavli Institute for Cosmology, University of Cambridge, Madingley Road, Cambridge CB3 0HA, UK*

[60]*David A. Dunlap Department of Astronomy & Astrophysics,*
University of Toronto, 50 St. George St., Toronto, ON, M5S 3H4, Canada

[61]*School of Mathematics and Physics, University of Queensland, Brisbane, QLD 4072, Australia*

[62]*Department of Physics and Astronomy, Rutgers, the State University of New Jersey,*
136 Frelinghuysen Road, Piscataway, NJ 08854-8019, USA

[63]*Center for Astrophysics | Harvard & Smithsonian, 60 Garden Street, Cambridge, MA 02138, USA*

[64]*Australian Astronomical Optics, Macquarie University, North Ryde, NSW 2113, Australia*

[65]*Lowell Observatory, 1400 Mars Hill Rd, Flagstaff, AZ 86001, USA*

[66]*Centre for Gravitational Astrophysics, College of Science,*
The Australian National University, ACT 2601, Australia

[67]*The Research School of Astronomy and Astrophysics, Australian National University, ACT 2601, Australia*

[68]*Departamento de Física Matemática, Instituto de Física,*
Universidade de São Paulo, CP 66318, São Paulo, SP, 05314-970, Brazil

[69]*Dunlap Institute of Astronomy & Astrophysics, 50 St. George St., Toronto, ON, M5S 3H4, Canada*

[70]*Perimeter Institute for Theoretical Physics,*
31 Caroline Street N, Waterloo ON N2L 2Y5 Canada

[71]*George P. and Cynthia Woods Mitchell Institute for Fundamental Physics and Astronomy,*
and Department of Physics and Astronomy, Texas A&M University, College Station, TX 77843, USA

[72]*Department of Astronomy and Astrophysics, University of Chicago, 5640 S. Ellis Ave., Chicago, IL 60637, USA*

[73]*Kavli Institute for Cosmological Physics, University of Chicago, 5640 S. Ellis Ave., Chicago, IL 60637, USA*

[74]*Department of Physics, University of Chicago, Chicago, IL 60637, USA*

[75]*Enrico Fermi Institute, University of Chicago, Chicago, IL 60637, USA*

[76]*Astrophysics Research Centre, University of KwaZulu-Natal, Westville Campus, Durban 4041, South Africa*

[77]*School of Mathematics, Statistics & Computer Science,*
University of KwaZulu-Natal, Westville Campus, Durban4041, South Africa

[78]*Max Planck Institute for Extraterrestrial Physics, Giessenbachstrasse, 85748 Garching, Germany*

[79]*Department of Physics, University of Milano-Bicocca, Piazza della Scienza 3, 20126 Milano (MI), Italy*

[80]*Kavli Institute at Cornell for Nanoscale Science, Cornell University, Ithaca, NY 14853, USA*

[81]*Department of Physics and Astronomy, Pevensey Building, University of Sussex, Brighton, BN1 9QH, UK*

[82]*Brookhaven National Laboratory, Bldg 510, Upton, NY 11973, USA*

[83]*Department of Applied Mathematics and Theoretical Physics,*
University of Cambridge, Cambridge CB3 0WA, UK

[84]*Instituto de Física, Pontificia Universidad Católica de Valparaíso, Casilla 4059, Valparaíso, Chile*

[85]*School of Physics and Astronomy, University of Southampton, Southampton, SO17 1BJ, UK*

[86]*Center for Computational Astrophysics, Flatiron Institute, NY NY 10010, USA*

[87]*Department of Astrophysical Sciences, Princeton University, Princeton NJ 08544, USA*

[88]*Computer Science and Mathematics Division, Oak Ridge National Laboratory, Oak Ridge, TN 37831*

[89]*Institute of Cosmology and Gravitation, University of Portsmouth, Portsmouth, PO1 3FX, UK*

[90]*Universitäts-Sternwarte, Fakultät für Physik, Ludwig-Maximilians Universität München, Scheinerstr. 1, 81679 München, Germany*
[91]*NASA Goddard Space Flight Center, 8800 Greenbelt Rd, Greenbelt, MD 20771, United States*
[92]*MIT Kavli Institute, Massachusetts Institute of Technology,*
77 Massachusetts Avenue, Cambridge, MA 02139, USA

We present a tomographic measurement of the cross-correlation between thermal Sunyaev-Zeldovich (tSZ) maps from *Planck* and the Atacama Cosmology Telescope (ACT) and weak galaxy lensing shears measured during the first three years of observations of the Dark Energy Survey (DES Y3). This correlation is sensitive to the thermal energy in baryons over a wide redshift range, and is therefore a powerful probe of astrophysical feedback. We detect the correlation at a statistical significance of 21σ, the highest significance to date. We examine the tSZ maps for potential contaminants, including cosmic infrared background (CIB) and radio sources, finding that CIB has a substantial impact on our measurements and must be taken into account in our analysis. We use the cross-correlation measurements to test different feedback models. In particular, we model the tSZ using several different pressure profile models calibrated against hydrodynamical simulations. Our analysis marginalises over redshift uncertainties, shear calibration biases, and intrinsic alignment effects. We also marginalise over Ω_m and σ_8 using *Planck* or DES priors. We find that the data prefers the model with a low amplitude of the pressure profile at small scales, compatible with a scenario with strong AGN feedback and ejection of gas from the inner part of the halos. When using a more flexible model for the shear profile, constraints are weaker, and the data cannot discriminate between different baryonic prescriptions.

I. INTRODUCTION

The Cosmic Microwave Background (CMB) provides a means to study early Universe physics as well as a powerful tool with which to probe the properties of the late Universe. As photons travel through cosmic time, they are affected by the large-scale structure of the Universe at low redshift, which leaves an imprint on the CMB. Among these so called "secondary anisotropies," generated after photons leave the surface of last scattering, the imprints left by the thermal Sunyaev–Zel'dovich (tSZ) effect [83, 84] are some of the most important. The effect is caused by inverse Compton scattering of CMB photons with ionised gas. The tSZ effect is an effective probe of large-scale structure, as the signal is sensitive to the halo mass function, which in turn strongly depends on the amplitude of the matter fluctuations, i.e., σ_8, and on the matter density, Ω_m [39]. It is also an effective probe of the properties of the hot gas within and outside dark matter halos, as the measured signal depends on the hot gas pressure profile.

A better understanding of the properties of baryons within dark matter halos is needed to fully exploit the cosmological information from the small-scale regime in current and future cosmological analyses (DES, Flaugher et al. [17]; KIDS, Kuijken et al. [41]; HSC, Aihara et al. [2]; Rubin LSST, LSST Science Collaboration et al. [45]; Euclid, Laureijs et al. [42]). Astrophysical feedback significantly impacts the baryons, leading to changes in the matter power spectrum at small scales [10, 88, 89]. Ignoring such effects can lead to significant biases in cosmological analyses [16, 32, 76].

Various strategies have been adopted to mitigate the impact of baryonic feedback on cosmological constraints. The most straightforward way is to exclude the scales that could be significantly affected by baryonic effects (e.g., Troxel et al. [87]). Other methods include adding extra complexity to the modelling to account for the effect of baryons [3, 26, 37, 51, 52], empirically modelling baryonic effects using fitting formu-

lae calibrated against hydrodynamical simulations [25], or using principal component analysis and hydrodynamical simulations to identify the modes of the data vector most sensitive to baryonic effects, and to marginalise over them [16, 32, 33]. As many of these mitigation strategies rely more or less directly on hydrodynamical simulations, the specific details of the implementation of baryonic physics in such simulations also have an impact on these methods.

Analysis of the tSZ effect provides a potential means for setting priors on different baryonic feedback prescriptions, or to promote or rule out some of the hydrodynamical simulations. Particularly appealing are studies that involve the cross-correlation of the tSZ effect with other probes sensitive to large-scale structure. Such cross-correlations have different sensitivity to nuisance parameters that makes these measurements less prone to systematics. Moreover, cross-correlations with different probes are key to study the evolution of baryonic effects with redshift or their dependence on the environment and the halo mass. In this work we focus on cross-correlations between the tSZ effect and weak gravitational lensing, a measurement that has gained attention over the last few years. Van Waerbeke et al. [90] obtained the first detection of the cross correlation signal between the shear field and a Compton-*y* measurement, using a Canada France Hawaii Telescope (CFHT) lensing convergence map and a Compton-*y* map built using *Planck* data. In the following year, Hill & Spergel [28] measured the tSZ x CMB lensing signal for the first time, which is in spirit a similar measurement, although it probes a higher redshift range compared to [90]. Subsequently, other measurements have been performed by Hojjati et al. [30], who detected a cross-correlation signal using *Planck* data and a shape catalog from the RCSLenS survey, and by Osato et al. [60] using *Planck* and HSC data. For this work, we use the fiducial shape catalog for the DES Y3 data [19], and Compton-*y* maps from both *Planck* [68] and the Atacama Cosmology Telescope ACT [48].[1] The large area

---

* marcogatti29@gmail.com

[1] The ACT Compton-*y* map is created using both low (spatial) resolution data from *Planck* and high resolution data from ACT, but for the sake of simplicity we refer to it as the ACT map. More details are given in § II.

coverage by the DES Y3 weak lensing sample (4183 sq. degrees) allows us to considerably improve the signal-to-noise of the measurement compared to previous studies. Moreover, the addition of the ACT map — which covers a smaller area compared to *Planck* but has a much higher spatial resolution — allows us to extend the measurement down to ∼ 2.5 arcminutes scales.

In this work and in a companion paper (Pandey et al. [62], hereafter paper II) we present the correlation measurements and perform several different analyses. We focus here on two aspects in particular:

- we discuss various systematic tests, with a focus on the effect of potential contaminants, i.e. the cosmic infrared background (CIB), and radio sources;

- we compare the measurements to theoretical predictions using the halo model framework and pressure profiles as estimated from a number of hydrodynamical simulations, with the goal of discriminating between different baryonic feedback models.

The analysis performed in this paper treats the pressure profile predictions of hydrodynamical simulations as fixed, and fits the data marginalizing over several nuisance parameters, modelling astrophysical and measurement systematics, including photometric redshift uncertainties, intrinsic alignment and shear calibration biases. We also marginalise over cosmological parameters assuming *Planck* or DES priors. On the other hand, in paper II, we use an alternate approach:

- we fit the measurements by varying the parameters of a flexible model for the halo pressure profiles, exploring how the halo pressure profiles evolve as a function of halo mass and redshift;

- we discuss implications of our measurements on the constraints of the so-called halo mass bias parameter.

The paper is organised as follows. In § II we describe the data used in this work. § III describes the theoretical modelling of the measurement, introducing the feedback models considered in this work and the modelling choices of the analysis. § IV B presents our *Planck* x DES and ACT x DES measurements, and systematic tests are discussed in § IV C. We test different feedback models in § IV D; we summarise our findings in § V. We provide further validation of our modelling on N-body simulations in Appendix A; Appendix B shows our validation of the analytical covariance matrix; Appendix C illustrates the effect of CIB contamination on simulated Compton-*y* maps; last, Appendix D shows our results when DES priors for the cosmological parameters are assumed.

II.   DATA PRODUCTS

A.   Planck Compton map

We use the publicly available 2015 *Planck* High Frequency Instrument (HFI) and Low Frequency Instrument (LFI) maps

[65, 66] to estimate the Compton-*y* map using the Needlet Internal Linear Combination (NILC) algorithm [13, 20]. We build our own version of the *Planck* Compton-*y* map, also using different prescriptions to de-project (i.e., remove) the contamination by the cosmic infrared background (CIB).

In particular, we use all the channels from 30 GHz to 545 GHz. We do not include the frequency map at 857 GHz because (1) the calibration of this map is more uncertain than the other frequency maps; (2) the dust is much brighter in this map than in any of the other maps and there are large dust-related residuals found in NILC maps if the 857 GHz map is used [68]. We also estimate the Compton-*y* map excluding the 545 GHz channel to test the sensitivity of our results to the CIB, which is brightest at high frequencies. The details of the implementation of this algorithm are presented in Appendix A of Pandey et al. [61] and more details on the CIB contribution are given in § IV C. We found that the signal obtained using our own version of the Compton-*y* map with no CIB de-projection was compatible with the signal obtained using the public *Planck* Compton-*y* map [68]. The maps come in HEALPIX format with a resolution of NSIDE = 2048. The *Planck* *y*-map resolution has an effective Full-Width-Half-Maximum (FWHM) of 10 arcminutes. When producing the Compton-*y* maps, we applied the standard *Planck* foreground mask, which limits the diffuse Galactic emission removing the most-contaminated ∼40 per cent of the sky, mostly around the Galactic plane. We further applied the fiducial DES Y3 mask [77], which removes areas affected by astrophysical foregrounds (e.g., bright stars and large nearby galaxies) and 'bad' regions with recognised data processing issues within the DES Y3 footprint. In the fiducial maps we did not mask radio sources; however, for the purpose of testing, we produced an alternate version of the maps by removing the pixels affected by radio sources detected by ACT (which detects sources to a fainter limit compared to *Planck*). Lastly, we removed the regions that have overlap with ACT data, since that part of the sky is covered by the ACT + *Planck* Compton-*y* map (described in the next section) and the latter is preferred as it comes at a higher spatial resolution. In order to avoid correlations between the two Compton-*y* maps during the analysis, we further cut out a "buffer" region of a few degrees of width between the two maps, as shown in Fig. 1. This reduces the covariance between the measurements obtained using the two maps. The final area covered by *Planck* data is 3423 square degrees.

B.   ACT Compton map

We use Compton-*y* maps from the Atacama Cosmology Telescope (ACT), as presented in [48] as part of DR4. The maps are obtained by combining *Planck* maps from 30 to 545 GHz and ACT maps at 98 and 150 GHz, using an anisotropic ILC component separation approach in the 2D Fourier domain (slightly different from the one used to create *Planck* maps). The original ACT maps are converted to HEALPIX
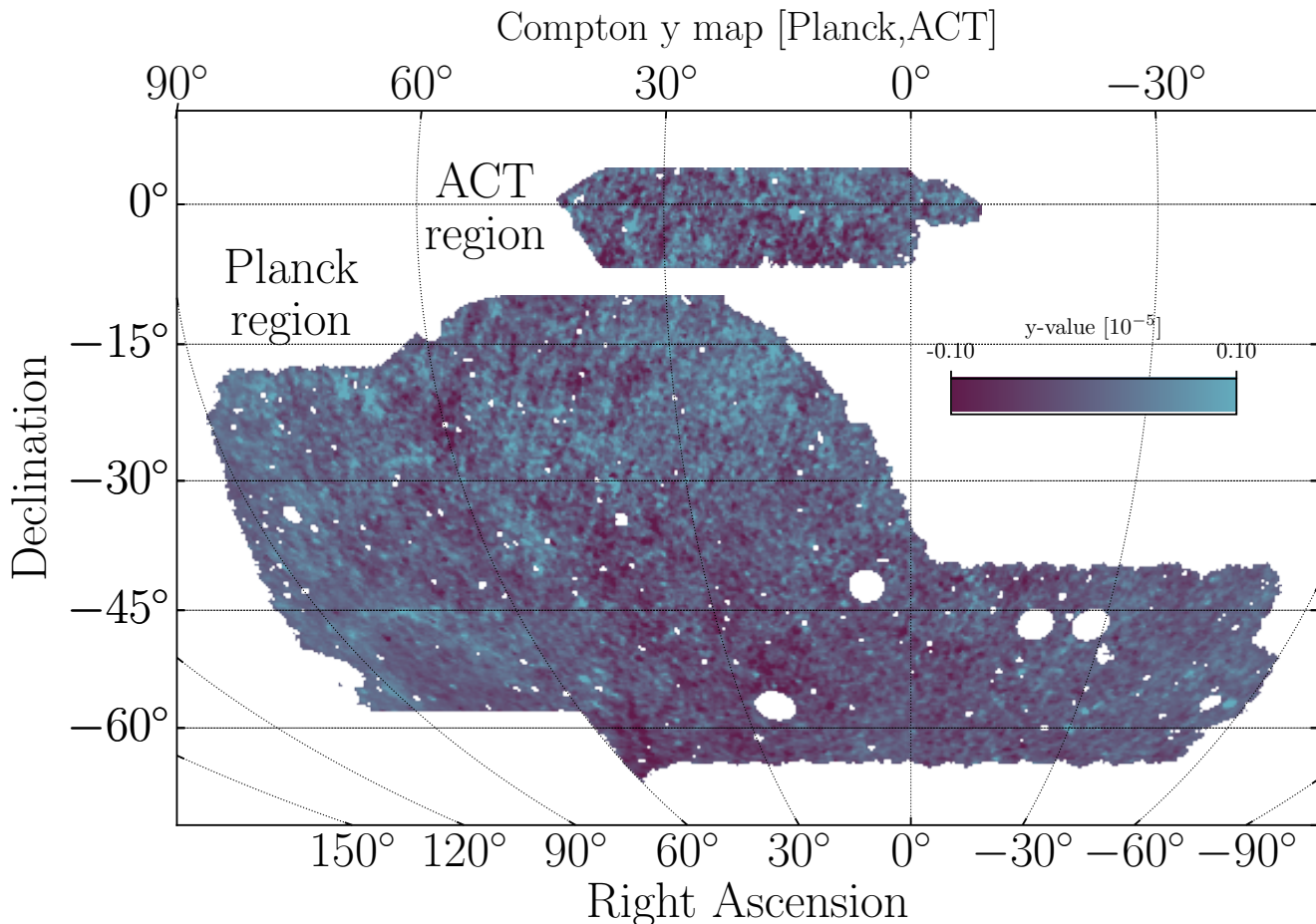
Figure 1. *Planck* and ACT Compton y-maps after isolating the part of the maps that overlap with the DES Y3 footprint. A small "buffer" region between the two maps has been removed to reduce correlation between measurements in the two patches.

format using the PIXELL package[2]; the maps have a resolution of NSIDE = 8192, with a FWHM of 1.6 arcminutes. We only use data from the D56 region, which overlaps with DES data, for a total area of 394 square degrees, after applying the ACT and DES masks. In contrast to the *Planck* maps case, for ACT compact sources (like radio sources) are subtracted by default, and the subtraction is followed by an inpainting procedure that estimates the correct value of the pixels affected by the compact sources. The inpainting algorithm fills holes around compact sources by finding the maximum-likelihood solution for pixels within the hole constrained by the pixels in a context region around the hole [48]. For the purpose of testing, we also make use of versions of the ACT map with the CIB contribution de-projected (see § IV C). Contrary to the *Planck* map we do not create a version of the ACT Compton-y map excluding the 545 GHz frequency channel, as the fiducial ACT maps already assign a very small weight to this frequency channel.

C. DES Y3 Data

We use the fiducial DES Y3 shape catalog, presented in [19]. The DES Y3 shape catalogue is created using the META-CALIBRATION pipeline, which is able to self-calibrate the measured shapes against shear and selection biases by measuring the mean shear and selection response matrix of the sample. The current DES Y3 implementation of METACALIBRATION [34, 78] is able to correct for shear biases up to a multiplicative factor of 2-3 per cent, which is fully characterised using image simulations [47]. The final sample comprises 100 million objects, for an effective number density of n_{eff} = 5.59 gal/arcmin^2, spanning an effective area of 4139 square degrees. Galaxies are further divided into 4 tomographic bins and redshift estimates for each of the tomographic bins are provided by the SOMPZ method [56]. The method uses additional information from deep fields [23] and spectroscopic samples to break degeneracies in the photo-*z* estimates of the wide field; this is achieved by creating self-organising maps (SOMs) of the spectroscopic, the deep and wide field galaxies and mapping the three together. The redshift bin edges of the tomographic bins used for the tomographic bin assignments are z = [0.0, 0.358, 0.631, 0.872, 2.0]; wide field galaxies

---

$$C_\ell^{\kappa,y;1h} = \int_{z_{\min}}^{z_{\max}} dz \frac{dV}{dz d\Omega} \int_{M_{\min}}^{M_{\max}} dM \frac{dn}{dM} \bar{\kappa}_\ell(M,z) \, \bar{y}_\ell(M,z),$$
(1)

where dV is the cosmological volume element, dn/dM is the halo mass function from [85], and $\bar{y}_\ell$ and $\bar{\kappa}_\ell$ are the harmonic space profiles of the Compton-y map and the lensing convergence, respectively. The two-halo term is given by

$$C_\ell^{\kappa,y;2h} = \int_{z_{\min}}^{z_{\max}} dz \frac{dV}{dz d\Omega} b_\ell^\kappa(z) \, b_\ell^y(z) \, P_{\lin}(k,z),$$
(2)

where $k = (\ell + 1/2)/\chi$, χ is the comoving distance to redshift z, $P_{\lin}(k,z)$ is the linear power spectrum, and b_ℓ^κ and b_ℓ^y are the effective linear bias parameters describing the clustering of the two tracers.

The total power spectrum is obtained by summing the 1-halo and 2-halo components:

$$C_\ell^{\kappa,y} = C_\ell^{\kappa,y;1h} + C_\ell^{\kappa,y;2h}.$$
(3)

The y-γ_t cross-correlation can then be written as (similar to [30] but without the flat-sky approximation):

$$\xi^{\gamma_t y}(\theta) = \int \frac{d\ell \, \ell}{2\pi} J_2(\ell\theta) C_\ell^{\kappa,y},$$
(4)

where J_2 is the second order Bessel function of the first kind.

A. The halo pressure profile

The profile in harmonic space of the Compton-y map can be related to the pressure profile $P_e(x|M_{200c},z)$ via (see, e.g., [27, 38, 39]):

$$\bar{y}_\ell(M_{200c},z) = b^j(\ell) \frac{4\pi r_{200c}}{l_{200c}^2} \frac{\sigma_T}{m_e c^2} \int_{x_{\min}}^{x_{\max}} dx \, x^2 \, P_e(x|M_{200c},z)$$
$$\times \frac{\sin(\ell x/l_{200c})}{\ell x/l_{200c}}. \quad (5)$$

In the above equation we have defined $x = a(z)R/R_{200c}$, where $a(z)$ is the scale factor, R is the radius and R_{200c} the radius enclosing the spherical region in which the average density is 200 times the critical density at the respective redshift; moreover, we defined $l_{200c} = D_A/R_{200c}$, where D_A is the angular diameter distance to redshift z. We choose $x_{\min} = 10^{-3}$ and $x_{\max} = 4$, which ensures that the above integral captures the contribution to the pressure from the extended profile of hot gas. Lastly, the term $b^j(\ell) = \exp[-\ell(\ell + 1)\sigma_j^2/2]$ captures the beam profile. Here $\sigma_j = \theta_j^{\mathrm{FWHM}}/\sqrt{8\ln 2}$ and we have $\theta_1^{\mathrm{FWHM}} = 10$ arcmin and $\theta_2^{\mathrm{FWHM}} = 1.6$ for *Planck* and ACT respectively. We note that since we are dealing with pixellised Compton-y maps, we should also take into account the pixel window function; in practice, since the size of the pixel is always smaller than $0.5\theta^{\mathrm{FWHM}}$, it can be safely neglected.

The effective tSZ bias b_ℓ^y is given by:

$$b_\ell^y(z) = \int_{M_{\min}}^{M_{\max}} dM \, \frac{dn}{dM} \bar{y}_\ell(M,z) b_{\lin}(M,z),$$
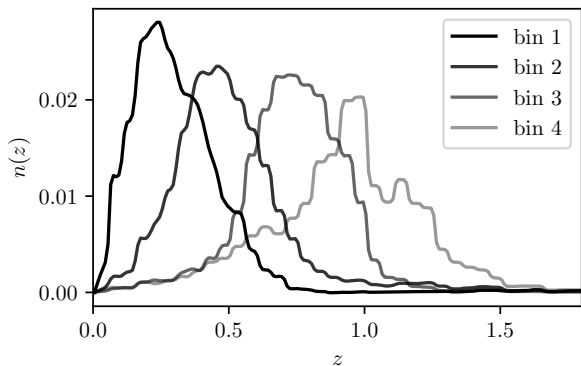(6)

Figure 2. Redshift distributions for the four DES Y3 tomographic bins [56].

are assigned to different tomographic bins depending on the mean redshift of the cell of the deep SOM they are associated to. This assignment procedure, however, does not guarantee that the redshift distributions are sharply bounded (Fig. 2) Throughout this paper, we use the fiducial DES Y3 priors for the shear calibration biases and redshift uncertainties (see § III D).

III. THEORY

There exist different tSZ-weak lensing cross-correlation estimators in the literature, both in configuration and harmonic space (for a discussion on different estimators see, e.g., [30]). Some of these estimators require construction of a weak lensing convergence map from shear field estimates as an intermediate step, which usually requires extra care in the modelling of the signal due to systematics and uncertainties introduced by the map reconstruction process. In this work, however, we focus on a configuration space estimator, the $\xi^{\gamma_t y}$ correlation function, which does not require this intermediate step. Given a catalog of galaxy shapes and a Compton-y map, such an estimator is constructed by measuring the tangential shear around every point of the y map, for different angular separations θ, and then averaging all the measurements. This estimator has the advantage of being particularly robust to additive systematics in the shear data. The measured $\xi^{\gamma_t y}$ correlation signal can be theoretically modelled relying on the halo model framework [11]. Note that the validity of the halo model to describe shear-Compton-y cross-correlation measurements has been demonstrated by [5], using hydrodynamical simulations [4].

We begin by modelling correlations between the convergence field and Compton-y maps in harmonic space, and then transform this model to obtain a prediction for the $\xi^{\gamma_t y}$ correlation signal in configuration space. In harmonic space, the correlation can be described as an effective sum of a one-halo term and a two-halo term, with the one-halo term given by an integral over redshift (z) and halo mass (M):
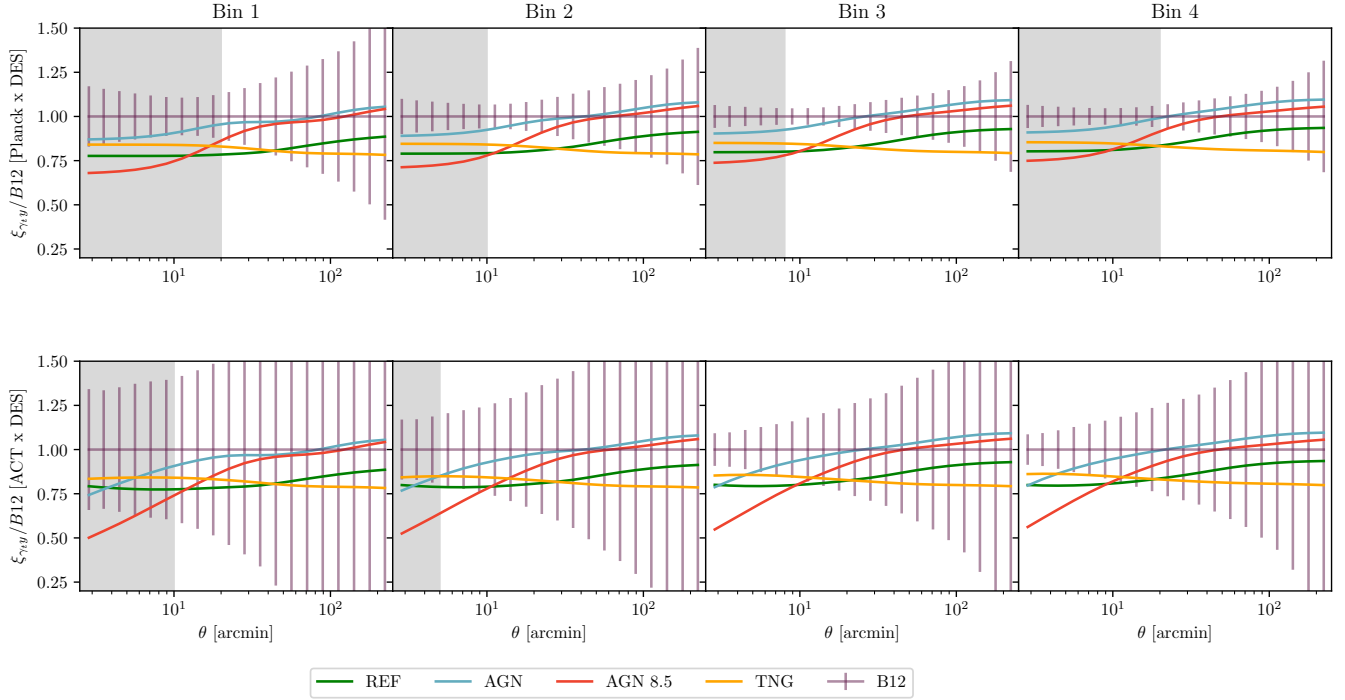
Figure 3. Differences in the expected $\xi^{\gamma_t y}$ correlation signals assuming different pressure profile models, as introduced in § III A. We take the predicted signal obtained with the B12 model as a reference. We show the predicted signals for the four tomographic bins of the DES shape catalog and for the two different Compton-y maps (ACT and *Planck*). For this figure, the shear part of the signal has been modelled assuming a Navarro–Frenk–White (NFW) profile for the DM profile. Error bars for the B12 model show the expected measurement uncertainties ACT measurement uncertainties are larger than *Planck* because of the smaller sky coverage. Grey shaded regions indicate the scales that are not used in this analysis (Table II). The error bars are strongly correlated between bins.
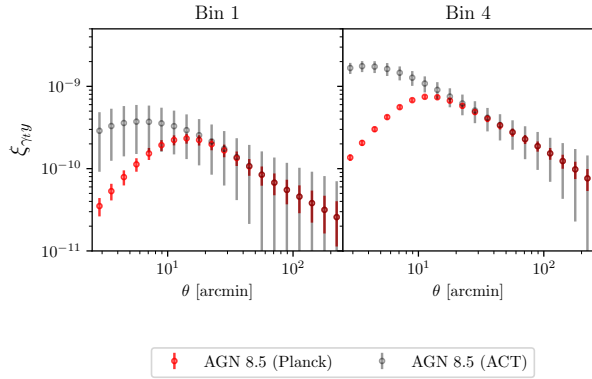

Figure 4. Expected $\xi^{\gamma_t y}$ correlation signals for the ACT x DES (grey) and *Planck* x DES (red) measurements, assuming AGN 8.5 feedback model, as introduced in § III A. We just show the first and the fourth bin; error bars represent measurement uncertainties. The dampening of the signal predicted for the *Planck* map at small scales is due to the large *Planck* beam.

plementing different baryonic feedback prescriptions:

- The Battaglia et al. [4] (B12) pressure profile, calibrated against a suite of hydrodynamical TreePM-SPH simulations that include radiative cooling, star formation, supernova feedback, and AGN feedback;

- The Le Brun et al. [43] REF model, calibrated against a version of the cosmo-OWLs simulations [44] that includes prescriptions for radiative cooling, stellar evolution, mass-loss, chemical enrichment and kinetic stellar feedback;

- The Le Brun et al. [43] AGN model, calibrated against a version of the cosmo-OWLs simulations that also includes a prescription for AGN feedback. In particular, we include the two variants, the AGN and AGN 8.5 models, with the latter being characterised by a stronger AGN feedback prescription;

- The pressure profile as measured in the IllustrisTNG simulation (TNG hereafter; Springel et al. [81]). The pressure profile is modelled as a generalised Navarro–Frenk–White (NFW) profile [58] similar to the B12 model, but fitting the model parameters (as well as their halo mass and redshift evolution) to the pressure profiles measured in the IllustrisTNG simula-

where b_{lin} is the linear bias of halos with mass M at redshift z (in the halo model, the halos are biased tracers of the underlying linear matter field). We use the Tinker et al. [86] fitting function for halo bias as a function of mass and redshift.

In this work, we consider the following pressure profile models, calibrated against hydrodynamical simulations im-

tion.[3]

These are a wide range of hydrodynamical simulations with (more or less) different AGN prescriptions (see, e.g. EAGLE simulation, [24], Horizon simulation, [10], BAHAMAS simulation [50], etc.); measuring and comparing to all the pressure profiles from these simulations goes beyond the scope of this work. Moreover, we believe the profiles considered here already span a sufficiently wide range of different feedback models.

It is important to note that we are not interested here in freeing the parameters of the pressure profile models developed by Battaglia et al. [4] and Le Brun et al. [43], but rather we want to use their best fit values to test whether the feedback mechanisms implemented in the simulations provide a good description of our measurement (within uncertainties). A different approach, where the pressure profile parameters are varied, is adopted in paper II.

We show how different pressure profile models translate to differences in the expected $\xi^{\gamma_t, y}$ correlation signals in Fig. 3 (see also Fig. 4 for the expected amplitude of the signal). Different predictions are obtained via Eq. 4, assuming fiducial values for all the ingredients of the modelling except for the pressure profiles. For this comparison, the shear part of the signal has been modelled assuming a NFW profile for the DM profile (we note, however, that when analysing our data we would also allow the DM profile to vary under the effects of baryons, as explained in the next section). We show the $\xi^{\gamma_t, y}$ correlation signals for the *Planck* and ACT Compton-y maps with the four tomographic bins of the DES shape catalog. The modelling of the *Planck* x DES and ACT x DES measurements differ only in the amplitude of the FWHM of the beam. We take the B12 model as a reference. The REF model is characterised by a $10 - 20\%$ lower amplitude at all angular scales and for all the different redshifts. In this model, a large fraction of halo baryons are able to cool and form stars, reducing the gas fraction and the tSZ amplitude. On the other hand, the two AGN models show a similar amplitude to the B12 model at large scales, but the most extreme AGN model (8.5) shows a significant lower amplitude (down to $\sim 40\%$ in the ACT x DES measurement) at small scales, related to the gas ejection from the halo due to AGN feedback. Lastly, the TNG AGN model, which is based on a different suite of simulations and different AGN feedback mechanism compared to all the other models, is characterised by a 20% lower amplitude at all scales. The TNG AGN feedback is neither able to heat up the gas as much as the B12 model, resulting in a lower amplitude at all scales, nor to eject the gas from the halo as efficiently as the most extreme AGN 8.5 scenario (which would cause a lower amplitude at small scales).

---

[3] In particular, we followed [55] and measured the pressure profile parameters dividing the halos of the simulations in two halo mass bins (M$\sim 10^{13.5} - 10^{14.25}$ $M_\odot$ M$\sim 10^{14.25} - 10^{15.0}$ $M_\odot$, and at three different redshift ($z = 0, 0.31, 0.6$), and interpolated the mass/redshift dependence. We could not use more bins due to the paucity of halos in this mass and redshift range.

B. Shear signal

The lensing part of our signal is described by the profile of the lensing convergence in harmonic space:

$$\bar{\kappa}_\ell(M_{\rm vir}, z) = \frac{W^\kappa(z)}{\chi^2} u_{\rm m}(k, M_{\rm vir}), \qquad (7)$$

where $k = (\ell + 1/2)/\chi$ and $u_m(k, M)$ is the Fourier transformation of the dark matter density profile. The quantity $W^\kappa(z(\chi))$ is the lensing kernel, given by:

$$W^\kappa(z(\chi)) = \frac{3H_0^2 \Omega_m}{2c^2} \frac{\chi}{a(\chi)} \int_\chi^\infty d\chi' n_\kappa(z(\chi')) \frac{dz}{d\chi'} \frac{\chi' - \chi}{\chi'}, \quad (8)$$

with n_κ the normalized redshift distribution of the source galaxies. The redshift distribution of the source galaxies peaks at significantly higher redshift compared to the sensitivity of our signal (see Fig. 2 of paper II); this implies that the dilution of the signal due to sources physically associated to foreground clusters [69, 79] is negligible. The effective lensing bias is:

$$b_\ell^\kappa(z) = \int_{M_{\rm min}}^{M_{\rm max}} dM \frac{dn}{dM} \bar{\kappa}_\ell(M, z) b_{\rm lin}(M, z), \qquad (9)$$

where $b_{\rm lin}$ is the linear bias of halos with mass M at redshift z which we model using the Tinker et al. [86] fitting function. In case of no feedback, the dark matter profile can be modelled by a simple NFW profile [58], but in practice baryonic feedback can affect the overall matter distribution and matter profile. To model this effect we take two approaches.

In a first approach, we simply re-scale the lensing profile by a mass-independent factor that reads:

$$\bar{\kappa}_\ell(M, z) \to \bar{\kappa}_\ell(M, z) \sqrt{\frac{P_{\rm DM+baryons}(k, z)}{P_{\rm DM}(k, z)}}, \qquad (10)$$

where $k = (\ell + 1/2)/\chi$, $P_{\rm DM}$ and $P_{\rm DM+baryons}$ are the power spectrum from a dark-matter only simulation and the power spectrum from a hydrodynamical simulation with dark-matter and a sub-grid prescription for baryonic effects. This approach is equivalent to the one assumed in some cosmic shear analyses, where the effect of baryonic feedback processes is taken into account by re-scaling the 3D matter power spectrum [25, 87]. When testing the REF, AGN and AGN 8.5 models, we re-scaled the lensing profile using the power spectra measured directly in the corresponding cosmo-OWLs simulations (as reported by van Daalen et al. [88]). The effect of the re-scaling for the REF model is below 1% at all scales, whereas for the AGN and AGN 8.5 models it mostly dampens the amplitude of $\xi^{\gamma_t, y}$ below 10 arcminutes, reaching a 10% dampening at 2.5 arcminutes for the AGN 8.5 model (which is the most affected model). For the B12 model we do not have at our disposal the 3D power spectra measured in the corresponding simulations with and without baryonic feedback; so we did not consider this model in this first approach.

In the second approach we model the effects of baryonic feedback on the lensing kernel with more flexibility. Instead of using a re-scaled version of the NFW profile, we

use the Mead model [53] to determine $u_m(k, M)$, the Fourier transformation of the dark matter density profile. The Mead model builds upon the NFW profile, but it adds additional freedom such that the model can capture the effect of baryonic physics on the internal structure of halos. This is achieved by adding two parameters: A_{Mead}, the amplitude of the concentration-mass relation, and η_{Mead}, the "halo bloating parameter", which produces a (mass dependent) expansion of the halo profile.[4] The NFW profile is still included in the Mead model parameter space, as well as the re-scaled versions of the NFW profile used in the aforementioned approach. Full expressions for $u_m(k, M)$ and for the effective linear bias parameter $b_\ell^\kappa(z)$ of the Mead model are provided in paper II. In this second approach, when testing different feedback models, we marginalise over A_{Mead} and η_{Mead} using wide priors (similar to the ones assumed by [46]). This is more conservative than re-scaling the NFW profile using the power spectra measured in hydrodynamical simulations. Indeed, in the first approach we assumed the re-scaling of the lensing kernel to be independent of halo mass; our measurement, however, is mostly sensitive to $M_{200c} \sim 10^{14} \, M_\odot$ see paper II), so if the effect of baryonic feedback models were halo mass dependent, the re-scaling might be not accurate. By marginalising over the Mead model parameters, we let the data re-scale the lensing profile by the "right" amount. Note that *a priori* there should be a relation between the Mead halo model parameters and the pressure profile parameters, as we expect baryonic processes to have a simultaneous impact on the matter and gas. As the Mead halo model implemented in this work is an heuristic model, it is hard to place physically motivated priors on such a relation; therefore, we consider the Mead model and the pressure profile parameters as independent. In this respect, a more coherent frameworks (e.g., [54]) where the shear and tSZ signals are modelled starting from the distribution of gas, matter and stars can provide better insights into the interplay between the pressure and matter profiles in the presence of baryonic feedback processes.

We provide in Appendix A further validation of our modelling by measuring the shear-Compton-y map cross correlation on the fiducial DES Y3 N-body simulations.

C. Astrophysical and nuisance parameters

Astrophysical and measurement systematic effects are modelled through nuisance parameters. When performing our analysis, we marginalise over all the nuisance parameters. Values and priors are summarised in Table I.

Photometric redshift uncertainties. Uncertainties in the photometric redshift estimates from the SOMPZ method for the 4 tomographic bins of the weak lensing sample are

[4] We note that in [53], the authors provide best-fit values for the parameters A_{Mead} and η_{Mead} for a number of hydrodynamical simulations, as well as suggesting a relation between the two. We cannot use those values or such a relation here, as our implementation of the Mead model is slightly different from the one presented in [53], which is *optimised* for a cosmic shear analysis.

Table I. Cosmological, systematic and astrophysical parameters. The cosmological parameters considered are Ω_{m}, σ_8, Ω_{b} (the baryonic density in units of the critical density), n_s (the spectral index of primordial density fluctuations) and h (the dimensionless Hubble parameter). The nuisance parameters are the multiplicative shear biases m_i and the photometric uncertainties in the mean of the weak lensing samples Δz_i. The astrophysical parameters $A_{\mathrm{IA},0}$ and α_{IA} describe the intrinsic alignment model, whereas A_{MEAD} and η_{MEAD} are the Mead halo model parameters. The column "range" indicates the parameters space spanned when sampling the parameters posterior during the analysis. We report the boundaries for both Flat and Gaussian priors. For Gaussian priors we also report the mean and the σ values in the prior column. Priors are described in § III D.

Parameter	Range	Prior
Ω_{m} [*Planck*]	0.2...0.4	0.315 ± 0.007
σ_8 [*Planck*]	0.6...1.1	0.811 ± 0.006
Ω_{m} [DES]	0.2...0.4	0.27 ± 0.02
σ_8 [DES]	0.6...1.1	0.82 ± 0.05
h	Fixed	0.674
n_s	Fixed	0.965
Ω_{b}	Fixed	0.0493
$\Delta m_1 \times 10^2$	$-10.0...10.0$	-0.63 ± 0.91
$\Delta m_2 \times 10^2$	$-10.0...10.0$	-1.98 ± 0.78
$\Delta m_3 \times 10^2$	$-10.0...10.0$	-2.41 ± 0.76
$\Delta m_4 \times 10^2$	$-10.0...10.0$	-3.69 ± 0.76
$\Delta z_1 \times 10^2$	$-10.0...10.0$	0.0 ± 1.8
$\Delta z_2 \times 10^2$	$-10.0...10.0$	0.0 ± 1.5
$\Delta z_3 \times 10^2$	$-10.0...10.0$	0.0 ± 1.1
$\Delta z_4 \times 10^2$	$-10.0...10.0$	0.0 ± 1.7
$A_{\mathrm{IA},0}$	$-5.0...5.0$	0.49 ± 0.15
$\eta\mathrm{IA}$	$-5.0...5.0$	Flat
A_{MEAD}	$-5.0...5.0$	Flat
η_{MEAD}	0...1.0	Flat

parametrised through a shift Δz in the mean of the redshift distributions:

$$n^i(z) = \hat{n}^i(z - \Delta z), \qquad (11)$$

where $\hat{n}^i$ is the original estimate of the redshift distribution coming from the photometric redshift code for the bin i. This parameterisation of the redshift uncertainties has shown to be adequate for the DES Y3 analysis [12]. We assume DES Y3 Gaussian priors for the shift parameters.

Multiplicative shear biases. Biases coming from the shear measurement pipeline are modelled through an average multiplicative parameter $1 + m^i$ for each tomographic bin i, which affects our measurement as $\xi_t^{\gamma_t y} \to (1 + m^i)\xi_t^{\gamma_t y}$. Gaussian priors are assumed for each of the m^i, and have been estimated in [47]. The major contribution to the shear multiplicative bias comes from blending effects due to source crowding.

Intrinsic galaxy alignments (IA). IA has been neglected in all the previous works on shear-Compton-y cross-correlations. In theory, an IA contribution is expected, as Compton-y maps trace the underlying dark matter density

Table II. Angular scales considered for the analysis (in arcmin). More details are provided in § III D.

	bin 1	bin 2	bin 3	bin 4
Planck x DES	20'-250'	8'-250'	8-250	20'-250'
ACT x DES	10'-250'	5'-250'	2.5'-250'	2.5'-250'

field. Our implementation of the IA model follows the non-linear alignment (NLA) model [8, 29]. It can be easily incorporated in the modelling by modifying the lensing kernel (Eq. 8):

$$W^\kappa(\chi) \to W^\kappa(\chi) - A(z(\chi))n_\kappa(z(\chi))\frac{dz}{d\chi}. \quad (12)$$

The amplitude of the IA contribution can be written as a power-law:

$$A(z) = A_{IA,0}\left(\frac{1+z}{1+z_0}\right)^{\eta_{IA}}\frac{c_1\rho_{m,0}}{D(z)}, \quad (13)$$

with $z_0 = 0.62$, $c_1\rho_{m,0} = 0.0134$ ([8], [40]) and $D(z)$ the linear growth factor. We marginalise over $A_{IA,0}$ and η_{IA} assuming the constraints from the DES Y1 3x2 analysis. More details about the IA model, and its relative strength compared to the Compton-y-shear signal, are given in paper II.

We also tested an additional 1-halo IA contribution due to satellite galaxies alignment, following [18]. This extra contribution requires modelling the Halo Occupation Distribution (HOD) of satellite galaxies and the fraction of satellites as a function of redshift, which are somewhat uncertain for the DES Y3 weak lensing sample. For this reason, we decided to remove scales where this extra 1-halo model could provide a significant contribution. More details are given in paper II.

D. Likelihood and Covariance

Our data vector includes shear-Compton y-map correlations $\xi^{\gamma_t y}$ from both *Planck* and ACT maps. In both cases, we cross-correlated the maps with the four DES Y3 tomographic bins, for a total of 8 correlation measurements. We measured the cross-correlations in 20 bins (equally spaced in logarithmic scale) between 2.5 and 250 arcmin. We exclude some angular scales from our analysis, based on three different criteria: (1) we exclude all the scales below 8 arcmin for the *Planck* measurement, since these scales are well below the *Planck* beam size; (2) we remove small scales where our IA modelling might be inadequate (see paper II); (3) we remove scales that might be significantly affected by cosmic infrared background (CIB) contamination (see § IV C). Depending on the tomographic bin, we consider the most stringent criteria among these three. We summarise the scale cuts in Table II. Having defined our data vector, in order to test our models, we evaluate the posterior of the parameters conditional on the data by assuming a multivariate Gaussian likelihood for the data, i.e.

$$\ln\mathcal{L}(\mathcal{D}|\Theta) = -\frac{1}{2}(\vec{\mathcal{D}} - \vec{\mathcal{T}}(\Theta))\mathbb{C}^{-1}(\vec{\mathcal{D}} - \vec{\mathcal{T}}(\Theta))^T. \quad (14)$$

Here, $\vec{\mathcal{D}}$ is the measured $\xi_{\gamma_t y}$ data vector of length N_{data}, $\vec{\mathcal{T}}$ is the theoretical model for the data vector at the parameter values given by Θ, and $\mathbb{C}^{-1}$ is the inverse covariance matrix of shape $N_{data} \times N_{data}$. The measurement covariance is modelled from theory, including both a Gaussian and a non Gaussian term; we provide a detailed description in Appendix B, along with validation based on data and simulations. The posterior is then the product of the likelihood and the priors:

$$\mathcal{P}(\Theta|\mathcal{D}) = \frac{\mathcal{L}(\mathcal{D}|\Theta)P(\Theta)}{P(\mathcal{D})} \quad (15)$$

where the $P(\Theta)$ are the priors on the parameters of our model, and $P(\mathcal{D})$ is the evidence of data. To sample the posteriors of our parameters, we use the POLYCHORD sampler [21, 22], which is a nested sampler that uses slice sampling to sample within the nested iso-likelihood contours.

For the cosmological parameters, we assume a flat ΛCDM cosmology and vary two parameters: Ω_m and σ_8, leaving Ω_b (the baryonic density in units of the critical density), n_s (the spectral index of primordial density fluctuations) and h (the dimensionless Hubble parameter) fixed to values from Planck Collaboration et al. [67]. For Ω_m and σ_8, and for each model under testing we run our analysis twice, with Gaussian priors centered in [67] and DES Y1 [1] values, with width equal to the 1σ uncertainty on the two parameters from the two analyses, respectively. We used DES Y1 priors as at the time of writing the DES Y3 analysis had not been released yet. We also marginalise over nuisance parameters describing photo-z uncertainties, shear biases and IA effects in our measurements. We use fiducial DES Y3 priors for the photo-z uncertainties and shear biases. As for the IA priors, we use a Gaussian prior on the amplitude of the signal as constrained by the DES Y1 3x2 analysis [73]. We also marginalise over the Mead halo model parameters A_{Mead} and η_{Mead} using broad flat priors.

All the parameters varied in this work and priors assumed are given in Table I. We discuss in detail the impact of the priors on our measurement in § IV D (see Fig. 12).

IV. RESULTS

We first present our measurement with the relevant systematic tests, and then we show the comparison with the theoretical predictions using the halo model framework and pressure profiles from hydrodynamical simulations.

A. TSZ-weak lensing cross-correlation estimator

Our estimator for the tSZ-weak lensing cross-correlation is the cross-correlation $\xi^{\gamma_t y}$, which is constructed starting from the DES catalog of galaxy shapes and from the ACT and *Planck* Compton-y maps. Concerning the Compton-y maps,

Table III. Measurements signal-to-noise ratio (SNR), defined as SNR = $\sqrt{\chi_{\text{null}} - d.o.f.}$, with $\chi_{\text{null}} = \xi^{\gamma_t y} C^{-1} \xi^{\gamma_t y}$. When computing the SNR we exclude scales $\theta < 8$ arcmin for the *Planck* measurement, as these scales are significantly smaller than the *Planck* beam.

bin	*Planck* x DES	ACT x DES	combined
bin 1	6.9	3.8	7.9
bin 2	11	3.2	12
bin 3	15	6.2	16
bin 4	15	7.5	17
all bins	19	9.3	21

we create a catalog of points using the coordinates of the centre of each `HEALPY` pixel of the maps. For each point we then consider the complex shear of a given galaxy in the DES catalog at an angular separation θ. We then compute the tangential component of the shear and multiply it by the Compton-y value. We average over all the galaxies at that angular separation and over all the points in the Compton-y maps. The DES catalog is divided into four tomographic bins, hence we measure 8 correlation functions in total. For the computation of the signal, we use `TreeCorr` [36].

B. Fiducial measurement

Our fiducial measurement, obtained by cross-correlating both the *Planck* and ACT Compton-y maps with the DES shape catalog, is presented in Fig. 5. For the *Planck* map, we used a version of the map where CIB contribution is deprojected (we provide more details in § IV C). From Fig. 4 it can be seen how the *Planck* beam suppresses all the small-scale information, which is retained in the ACT x DES measurement. At large scales the two measurements are consistent with each other, although the ACT x DES measurement is noisier. Since we removed the area from the *Planck* data of the DES footprint covered by ACT, the two datasets can be considered approximately independent. If we select only the large scales unaffected by the beams (e.g., $\theta > 20$ arcmin), the two measurements are consistent with each other with a p-value = 0.05 ($\chi^2 = 60$ for 44 $d.o.f.$).[5] As an additional check, we also repeated the measurement using the part of the *Planck* map in the ACT footprint, finding good agreement with the ACT measurement over the same area.

We report in Table III the statistical significance of our measurements. Despite the higher resolution and better small-scale constraints, the ACT x DES measurement delivers lower signal-to-noise ratio (SNR) than *Planck* x DES, due to the smaller sky coverage. The overall SNR for the combined measurement, considering the 4 tomographic bins together, is nonetheless improved with respect to the *Planck* only measurement, and it is equal to SNR = 21. Concern-

---

[5] We measured the p-value by computing the difference between the two signals and used a theory covariance to estimate the covariance for the measurements difference.

Table IV. Summary of the compatibility and systematic tests performed on our measurements. We report the χ^2 and the $d.o.f.$ for the difference between the *Planck* and ACT measurements, as well as the difference between the measurements obtained using CIB deprojected maps and without de-projection. Lastly, for the $\gamma_\times$ test we report the χ^2 of the null hypothesis (i.e., no signal). The number of $d.o.f$ varies depending on whether the covariance is a theory covariance (which is the case of *Planck*-ACT compatibility), or a jackknife covariance (all the other cases), since for the latter case only the scales where the covariances is reliable have been used.

Test	$\chi^2/d.o.f.$
Planck-ACT compatibility, all bins	60/44
Planck, CIB, bin 1	4/8
Planck, CIB, bin 2	12/8
Planck, CIB, bin 3	55/8
Planck, CIB, bin 4	110/8
ACT, CIB, bin 1	4/8
ACT, CIB, bin 2	8/8
ACT, CIB, bin 3	14/8
ACT, CIB, bin 4	9/8
Planck radio contamination	34/32
Planck, $\gamma_\times$, all bins	84/68
ACT, $\gamma_\times$, all bins	93/80

ing the individual tomographic bins, the highest SNR is provided by the correlation with the two tomographic bins with the highest redshift. The effective redshift interval probed by these two correlations is $z \sim 0.3 - 0.5$ (see paper II). As a comparison, the first measurement of a cross-correlation between a CFHT convergence map and the *Planck* Compton-y map was detected at the $\sim 6\sigma$ C.L. [90]. A stronger detection was achieved by [30], who detected a cross-correlation signal at the $\sim 8.1\sigma$ C.L. for $\xi^{\gamma_t y}$ using *Planck* data and a shape catalog from the RCSLenS survey. Our measurement improves on this, owing to its larger sky coverage of the weak lensing data.

C. CIB contamination and systematic tests

We present here a number of tests to assess whether the Compton-y maps used in this work are affected by systematic effects. In particular, we are interested in the potential effect of two contaminants, namely, the cosmic infrared background (CIB) and radio point sources.

The CIB signal is sourced by thermal emission from galaxies over a broad range of redshift ($z \sim 0.1 - 4$), but with the bulk of the emission mostly peaking at high redshift ($z > 1$, Chiang et al. [9], Schmidt et al. [75]). By assuming an effective model for the main component of the CIB that is correlated across frequency, the CIB can be de-projected from the Compton-y map using the ILC method [72]. We model the effective CIB SED as a modified blackbody with "temperature" 24 K and spectral index β (following [48]). The parameters of this effective model do not correspond to the physical SED parameters of an actual infrared source, but
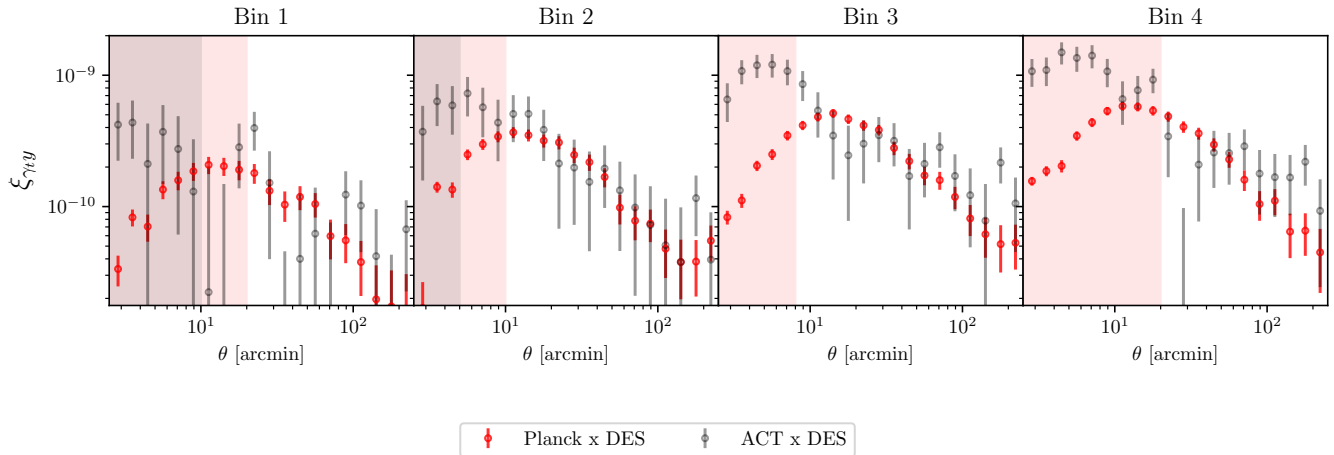
Figure 5. Measured shear-Compton-y cross-correlation $\xi^{\gamma_t y}$ from data (*Planck* x DES in red ACT x DES in grey). Error bars are taken to be the square-root of the diagonal of the theory covariance presented in Appendix B. The edges of the tomographic bins are [0.0, 0.358, 0.631, 0.872, 2.0], although we note that the redshift distributions are not sharply bounded (see § II C). We note that the difference at small scales between the *Planck* and ACT measurement is driven by the different beam size (the *Planck* map has a resolution of 10 arcminutes, whereas the ACT map has a resolution of 1.6 arcminutes). The effect of the *Planck* beam becomes negligible above 20 arcminutes, with the two measurements indeed showing a good agreement at large scales. Red shaded and grey shaded regions represent the scales removed from the main analysis, for the *Planck* x DES and ACT x DES measurements, respectively.

they do capture the frequency dependence seen in the sky-average CIB SED for the CIB halo model fit to the *Planck* CIB power spectra measurements. In this model the CIB emission rises quickly at high frequency and it is expected to mostly affect the frequency channel at 545 Ghz. We create three Compon-y maps using *Planck* frequency channels from 30 GHz to 545 GHz, de-projecting the CIB assuming the SED from [48] with slope $\beta = 1.0, 1.2, 1.4$[6]. In what follows, whenever needed, we will assume the value $\beta = 1.2$, and show the results for values $\beta = 1.0, 1.4$ only for comparison purposes. The value $\beta = 1.2$ is the one assumed in [48], obtained by comparison with *Planck* CIB halo model presented in [64]. The shear-Compton-y cross-correlation $\xi^{\gamma_t y}$ signal obtained using these maps is shown in Fig. 6, compared to the measurement obtained using the official *Planck* NILC Compton-y map presented in [68], which does not implement any CIB de-projection. Bins 3 and 4 are the ones where the measured signal is mostly affected by the CIB de-projection procedure, depending on the value of the SED slope β. We can quantify the effect of the CIB de-projection by measuring the significance of the difference between the signal obtained using the official *Planck* map and our de-projected maps. To this aim, we use a jackknife [59, 70] covariance (see Appendix B) for the measurement difference and restrict to the scales where the jackknife estimate is not affected by the limited size of the jackknife patches ($\theta < 40$ arcmin in this case). We note that such a covariance is smaller than the measurement covariance, because sample variance should largely

cancel when computing the difference between two signals measured over the same area.

This procedure is needed as the measurements involving the maps with and without CIB de-projections are highly correlated. When assuming $\beta = 1.2$, the χ^2 of the difference between the signals is $\chi^2 = 4$, $\chi^2 = 12$, $\chi^2 = 55$, $\chi^2 = 110$ for 8 *d.o.f.* for the 4 tomographic bins, respectively (Table IV). We further generate three additional *Planck* maps removing the 545 GHz frequency channel and assuming again $\beta = 1.0, 1.2, 1.4$. These are generally compatible with the ones including it (although they are noisier), except for the scales between $8 - 20$ arcminutes in bin 4 (middle panels of Fig. 6). Given these results, for the analysis presented in this work we decide to rely on the *Planck* Compton-y map obtained using all the frequency channels from 30 GHz to 545 GHz and with CIB de-projected using $\beta = 1.2$ for the CIB SED. We further decide to exclude in bin 4 scales $\theta < 20$ arcminutes, due to potential residual CIB contamination. Note that previous work on shear-Compton-y cross-correlation using the *Planck* Compton-y map suggested a weaker level of CIB contamination [91]. It is possible that the different redshift distribution of the galaxies used in this work could be responsible for a higher degree of CIB contamination compared to the work of [91]. In particular, the redshift distributions of our bin 3 and 4 peak at higher redshift with respect to the sample used in [91], overlapping more with the high redshift galaxies responsible for the bulk of the CIB emission. Additional discussion on the effects of CIB contamination using simulated Compton-y maps are provided in Appendix C. Lastly, we also show in Fig. 6 the effect of CIB de-projection on the cross-correlation $\xi^{\gamma_t y}$ signal obtained using the ACT maps. The effect is negligible here, as the χ^2 of the signals difference is compatible with noise: we obtain $\chi^2 = 4$, $\chi^2 = 8$, $\chi^2 = 14$, $\chi^2 = 9$ for 8 *d.o.f*, for scales $\theta < 15$ arcmin, for the

---

[6] We also tried with a larger value of $\beta = 1.6$, but found significantly increased uncertainties and no appreciable difference with respect to $\beta = 1.4$. This happens because $\beta = 1.6$ is a large value which does not describe well the data, and as a consequence, the CIB de-projection does not work properly.
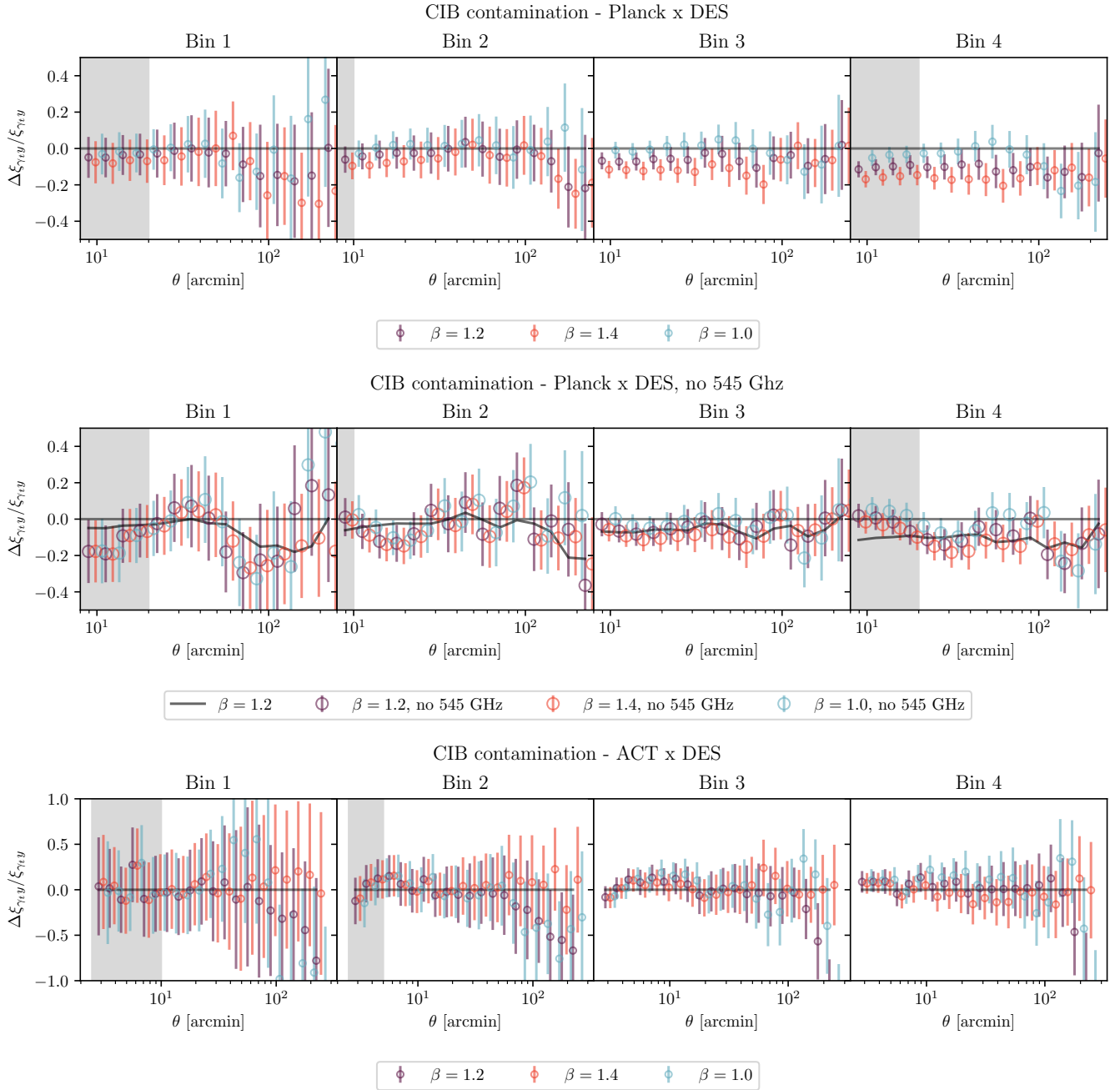
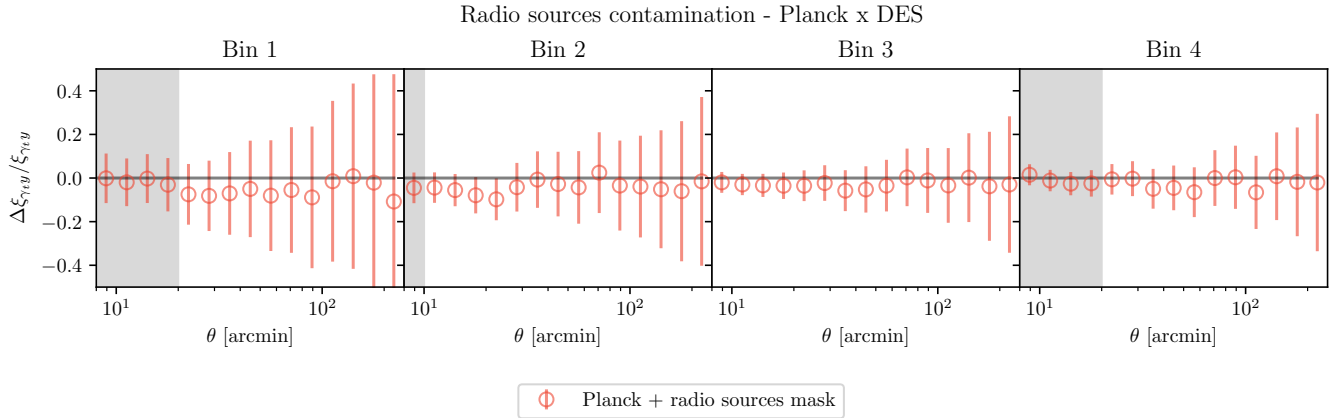Figure 6. Fractional difference in the measured shear-Compton-y cross-correlation $\xi^{\gamma_t y}$ when computed using the Compton-y map after de-projecting the CIB component, with respect to the map with no CIB de-projection. The upper plots show the results for the *Planck* maps created using all the frequency channels between 30 GHz and 545 GHz; the central plots show the results for the *Planck* maps excluding the 545 GHz frequency channel. In the central panels, the solid black line shows the $\beta = 1.2$ measurement when including the 545 GHz channel (from the upper panel plots) as a comparison. CIB has a strong impact on the *Planck* x DES measurements, especially for the ones involving the two highest redshift bins (see upper panel). CIB contamination is also seen when removing the 545 GHz frequency channel (central panels). The lower panels show the results for the ACT maps, which indicates negligible CIB contamination. Grey shaded regions represent the scales removed from the main analysis. The data are strongly correlated.

four tomographic bins (Table IV).[7] This is due to the ACT

---

[7] These χ^2 values are computed using as a covariance the measurements difference covariance, which is smaller than the covariance of a single mea-

surement due to cancelling sample variance. As a reference, if we were to compute the χ^2 of the signals difference using the single measurement covariance, we would obtain $\chi^2 \sim 2 - 3/8$ $d.o.f$

Figure 7. Fractional difference in the measured shear-Compton-y cross-correlation $\xi^{\gamma_t y}$ when computed using the *Planck* Compton-y map with and without masking radio sources. No statistically significant difference is measured, indicating no contamination due to radio sources. Grey shaded regions represent the scales removed in the main analysis.
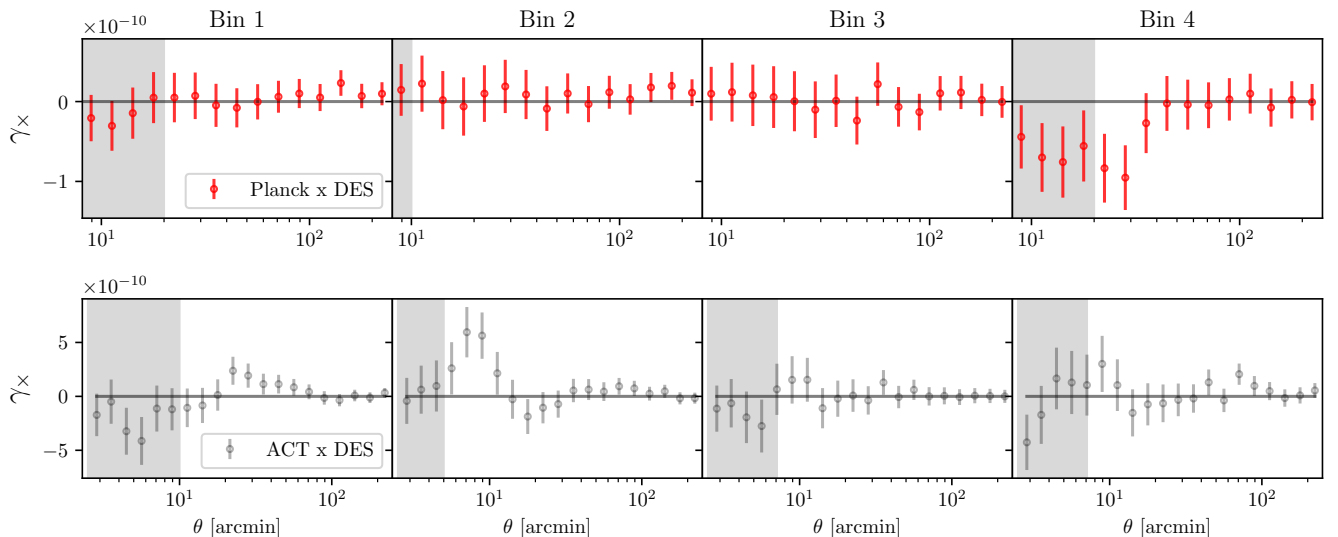

Figure 8. Cross-component of the lensing signal around points of the Compton-y maps. Grey shaded regions represent the scales removed in the main analysis. No statistically significant signal is measured (Table IV), indicating that the null test is passed. We note that the few points at ~ 10 arcmin for the second bin of the ACT x DES measurement that are showing a small deviation from zero are very correlated and are just a statistical fluke (we also tried to change the binning of the measurement finding again a null signal).

measurement being noisier than *Planck* (due to the smaller area coverage) and due to the ACT Compton-y map receiving significant contributions from the ACT 98 and 150 GHz channels (even on small scales), where the CIB is relatively faint. We also note that [74] found some evidence of mild CIB contamination for the ACT map only at scales smaller than 1 arminute, which are scales not considered in this work. Given the result of this test, in what follows, we will use the ACT map with no CIB de-projection.

As a second test, we proceed testing the potential contamination due to radio sources. Radio sources can potentially bias the signal at the 10-20% level [80], although the exact number depends on the SED and HOD of the radio sources, which are uncertain, and on the map making algorithm. Due to the uncertainties in the SED and HOD, the radio sources

contamination cannot be as easily de-projected as the CIB signal. The ACT map is created masking detected radio sources in every channel, and subsequently interpolating the map over the masked regions [48]; radio sources are usually detected down to 5-10 mJy. On the other hand, the *Planck* map used in this work does not have any radio sources mask applied by default. We therefore apply a radio sources mask to the *Planck* Compton-y map, using catalog of radio sources detected by ACT at 98 and 150 GHz. Such a catalog has not been released yet; it is built using ACT DR5 data and spans the full DES Y3 footprint [35]. Note that ACT can detect point-like radio sources much fainter than *Planck* (1-2 orders of magnitude fainter, depending on the *Planck* channel considered, Planck Collaboration et al. [63]). We masked a circular area of radius 10 arcmin around each source, and repeated

Table V. The MAP value of χ^2 for the feedback models, obtained assuming *Planck* priors on σ_8 and Ω_m, and marginalising over nuisance parameters as explained in § III D. The top half of the table refers to the models obtained re-scaling the NFW profile for the lensing signal; on the other hand, the bottom half of the table refers to the analysis where we model the lensing signal using the Mead model. We also report the update-difference-in-mean (UDM) tension for the best fit models with respect to their priors.

Planck prior (NFW re-scaling)					
	B12	**AGN**	**AGN 8.5**	**REF**	**TNG**
$\chi^2/d.o.f.$	-	172/119	158/119	189/119	198/119
UDM tension	-	4.5 σ	2.2 σ	3.3 σ	4.3 σ
Planck prior (free $A_{\text{Mead}}, \eta_{\text{Mead}}$)					
	B12	**AGN**	**AGN 8.5**	**REF**	**TNG**
$\chi^2/d.o.f.$	154/118	155/118	154/118	155/118	154/118
UDM tension	0.7 σ	1.5 σ	1.4 σ	0.5 σ	0.3 σ

the cross correlation measurement with the DES shape catalog. The masking reduced by 8% the area available for the cross correlation. The difference in the measurements (with and without radio sources mask applied) is shown in Fig. 7. No radio source signal is detected in the measurements difference: using the angular scales where the jackknife covariance is reliable, we obtained for the difference between the two signals $\chi^2/d.o.f = 34/32$, see Table IV. Given the lower signal-to-noise of the ACT measurement, and given the fact that this radio sources mask is already applied to the ACT map, we can also consider the impact of radio sources on the ACT map negligible.

As a last systematic test, we checked the cross-component of the mean shear around every point of the Compton-y maps. The cross-component is a standard null test in galaxy-galaxy lensing studies, as it should be compatible with zero if the shear is produced by gravitational lensing alone. The cross-component should also vanish in the presence of systematic effects that are invariant under parity. We test this in Fig. 8. Using a theory covariance, we obtain $\chi^2/d.o.f = 84/68$ and $\chi^2/d.o.f = 93/80$ for the *Planck* x DES and ACT x DES measurements (Table IV), respectively, indicating compatibility with a null signal and that the null test is passed.

D. Tests of feedback models

After characterising the measurement, we compare it to theoretical predictions using the halo model framework and pressure profiles as estimated from a number of hydrodynamical simulations. The pressure profiles and feedback models considered in this section are the five models introduced in § III A (B12, REF, AGN, AGN8.5, TNG). For the lensing part of the signal, we both model our theoretical predictions using the re-scaled NFW profiles and using the Mead model (§ III B). We compare our theoretical models to the measurement marginalising over a number of nuisance parameters modelling astrophysical and measurement systematics, including photometric redshift uncertainties, intrinsic align-

ment and shear calibration biases, as described in § III D. We also marginalise over σ_8 and Ω_m assuming *Planck* priors for the cosmological parameters (but we also repeat the analysis in Appendix D using DES Y1 priors). When using the Mead model for the lensing kernel, we also marginalise over Mead model parameters. Such marginalisation over systematics has generally been neglected in early works on weak lensing - tSZ correlations (but see Osato et al. [60]). When comparing models to the measurements, we always jointly fit the ACT x DES and *Planck* x DES measurements.

We start considering the analysis with re-scaled NFW profiles for the lensing part of the signal. This is the most constraining setup, as we do not marginalise over the effect of baryonic feedback on the matter profile, but rather we rely on the measurements of power spectra from hydrodynamic simulations to re-scale our theoretical predictions of the matter profile. Note that such re-scaling has a milder impact on the measurement compared to the effect of differences in the pressure profile from different hydrodynamical simulations. The main caveat of this approach is that such re-scaling neglects any halo mass dependency of the effect of baryonic feedback on the matter profile, as the power spectra do not carry an information about the halo mass, so it can be seen as an "effective" re-scaling. Note that due to the lack of the 3D power spectrum needed for the re-scaling for the B12 model, we did not consider it in this first part of the analysis.

Fig. 9 shows the *Maximum A Posteriori*, (MAP) models obtained by assuming the four feedback models and marginalising over nuisance and cosmological parameters. The pressure profiles are not varied, only the nuisance and cosmological parameters; so the best-fit models for our measurements are obtained using the pressure profiles from the hydrodynamical simulations and the best-fit nuisance and cosmological parameters from the analysis. The data likelihood at MAP are approximately described as a χ^2 distribution with $d.o.f.$ equal to the number of data points N_{points} minus the effective number of parameters N_{eff} constrained by our data compared to the priors it began with [71]. In our case $N_{\text{points}} = 123$, whereas the effective number is:

$$N_{\text{eff}} = N - \text{tr}[(C^p)^{-1} C^{p+d}], \qquad (16)$$

where C^p is the covariance of the prior, and C^{p+d} is the covariance of the prior updated by the data (i.e., the posterior). Moreover, $N = 12$, that is, the number of free 12 parameters in our analysis. We obtain, depending on the model, $N_{\text{eff}} \sim 4$. We note that although we free 12 parameters in our analysis, some of them are tightly constrained by their prior, such that $N_{\text{eff}} < 12$. The data likelihood at MAP is reported in Table V. The model that provides the MAP best fit χ^2 is the AGN 8.5 model, followed by the AGN 8, REF and the TNG model. In particular, the last two feedback models are penalised by the comparison with the ACT x DES data, which prefer the scenarios with a lower amplitude of the pressure profile at small scales, compatible with the ejection of gas from the inner part of the halo. On the other hand, the AGN 8.5 model also provides a better fit to the *Planck* x DES measurement at all scales (especially for bins 3 and 4) compared to the AGN model, hence providing the best χ^2 among all the scenarios probed here.
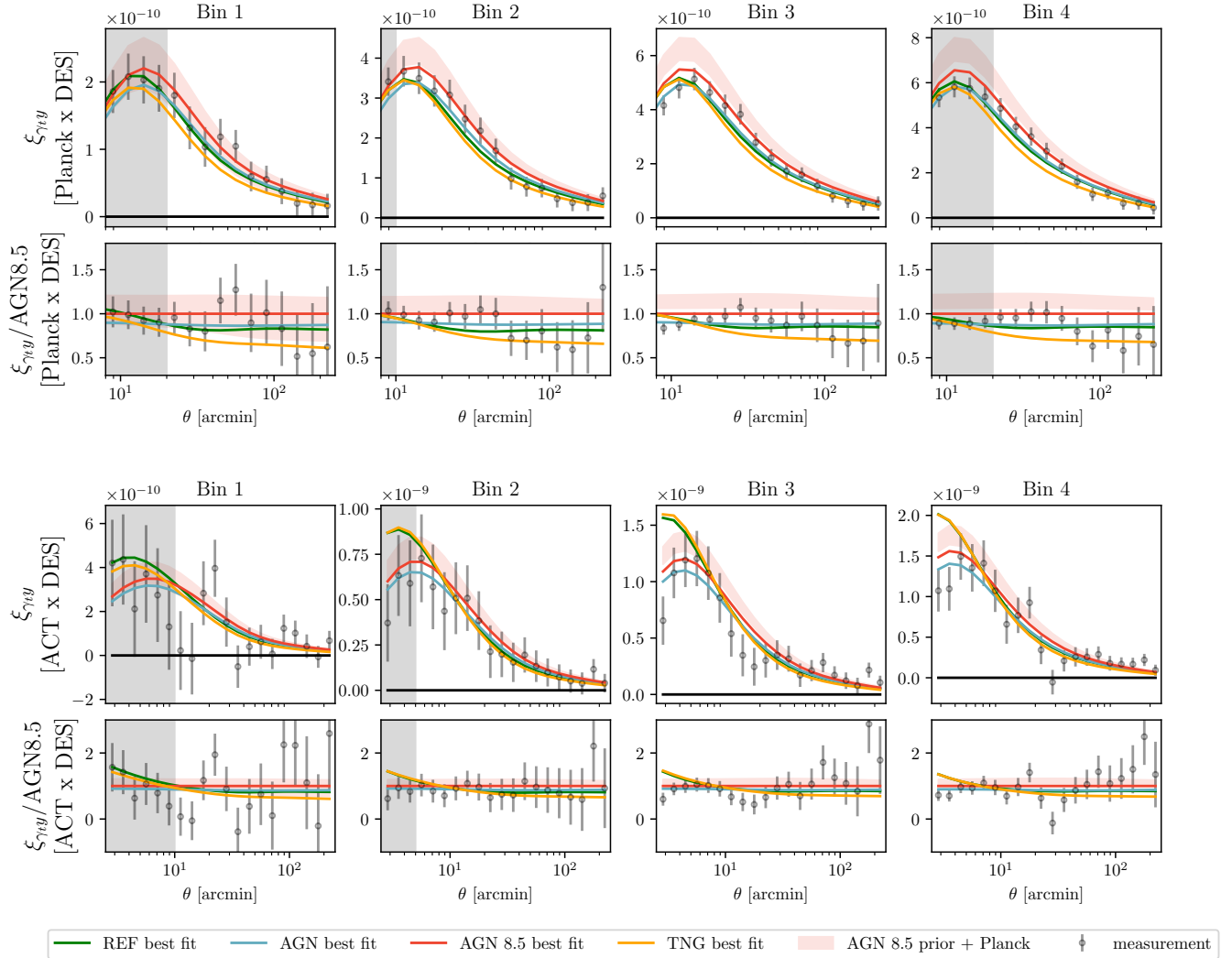
Figure 9. Measured shear-Compton-y cross-correlation $\xi^{\gamma_t y}$ and best fit models for four feedback models (TNG, AGN, AGN8.5 and REF). These models have been obtained assuming the re-scaled NFW profile for the lensing signal. Top panels show the cross correlations between *Planck* and DES Y3 data for the four tomographic bins, whereas bottom panels show the correlations between ACT and DES Y3 data. As a comparison, we also show as a coloured band encompassing the 68% confidence interval of the prior for the AGN 8.5 scenario. The grey shaded regions represent the angular scales not included in our analysis (see Table II.)

We compare if the best fit models are in tension with their priors. In order to quantify the level of agreement/disagreement we use a Gaussian estimator, called update difference-in-mean (UDM) statistic [71]. The UDM statistics compare the mean parameters from the prior $\hat{\theta}^p$ with the updated values $\hat{\theta}^{p+d}$ obtained running the analysis on data. This statistic assumes either flat or Gaussian priors (which is satisfied for all the parameters considered in this analysis, see Table I), and requires the posterior of the well-constrained parameters to be approximately Gaussian (which is also satisfied). In particular, we can define

$$Q_{\mathrm{UDM}} = (\hat{\theta}^{p+d} - \hat{\theta}^p)^T \left(C^p - C^{p+d}\right)^{-1} (\hat{\theta}^{p+d} - \hat{\theta}^p), \quad (17)$$

where the difference in the mean of the parameters $(\hat{\theta}^{p+d} - \hat{\theta}^p)$ is weighted by the parameters inverse covariance. If the pa-

rameters are Gaussian distributed, Q_{UDM} is chi-squared distributed with rank($C^{p+d} - C^p$) degrees of freedom. The UDM tension is reported in Table V. A tension would imply that for a *Planck* cosmological model, the tSZ signal that we measure is in tension with the predictions of these feedback models. For the AGN, REF and TNG models, the best fit are in tension at the 3-4 σ level with their priors, with the best-fit models to the data preferring different values of the cosmological parameters σ_8 and Ω_m than the ones measured by *Planck*. This is also shown in Fig. 10, which reports the posterior of the σ_8 and Ω_m parameters, compared to the priors used in the analysis.[8] On the other hand, the AGN 8.5 scenario, which is also the one the provides the best fit to the data, is not in

_____

[8] We caution the reader from "reading" the exact value of the UDM tension from Fig. 10: the posteriors are the results of the combination of the

Figure 11. Posterior for the Mead model parameters A_{Mead} and η_{Mead} for five feedback models: B12, REF, AGN, AGN 8.5 and TNG. The "star" indicates the values of the Mead models that best describes a NFW profile. The marginalised contours in this figure shows the 68% and 95% confidence levels.
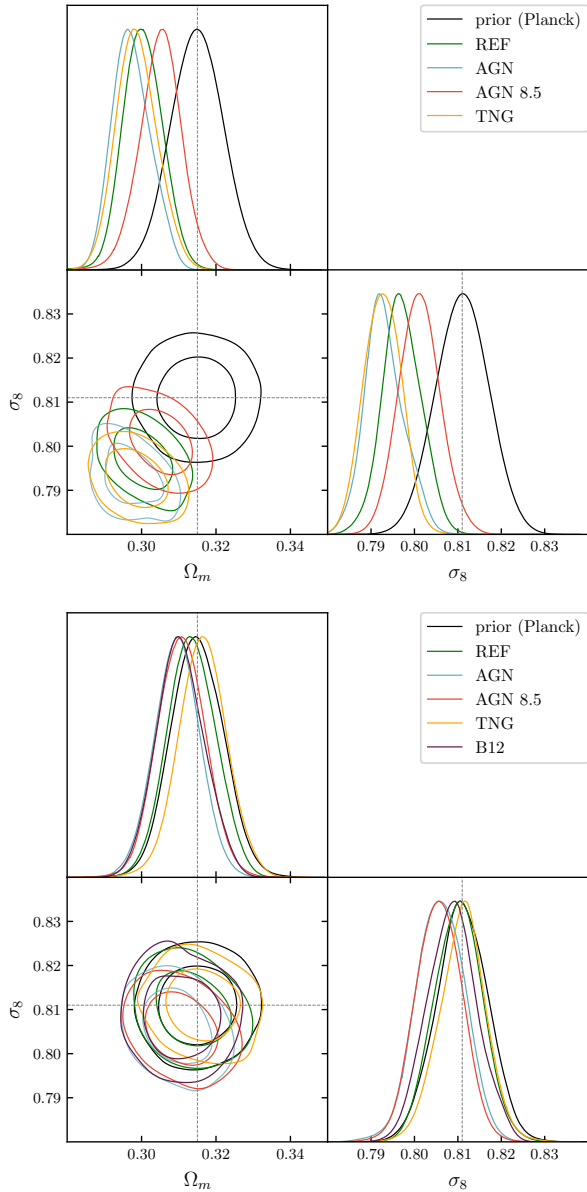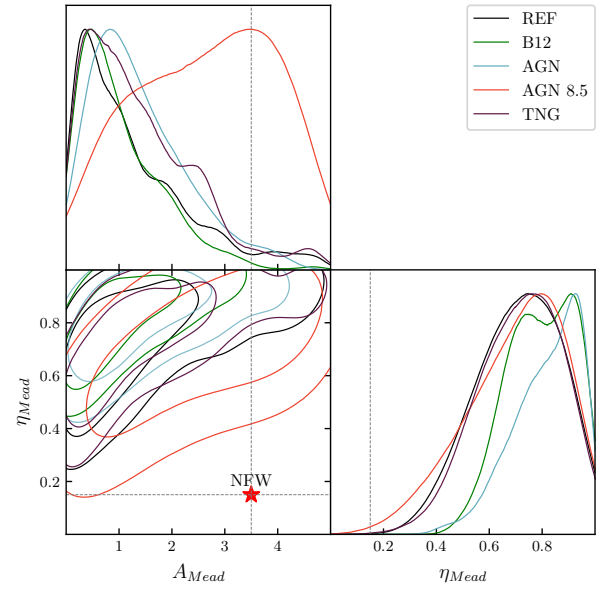

Figure 10. Posterior for the parameters σ_8 and Ω_m for the four (five) feedback models: (B12), REF, AGN, AGN 8.5 and TNG. We also show the *Planck* prior centered in each plot. Top refers to the case where we used the NFW re-scaling to model the lensing part of our signal; the bottom plot refers to the more conservative analysis where we used the Mead model. The marginalised contours in these figures show the 68% and 95% confidence levels. When the NFW re-scaling is used, the data are in mild to moderate tension with the *Planck* prior (2.2σ-4.5σ, see Table V).

Planck prior and the feedback models likelihood, whereas the UDM tension computes the tension between the model *alone* and the prior, which is in general larger than what it could be inferred "by-eye" from Fig. 10.

significant tension with its prior. Given the fact that the AGN 8.5 scenario is also the one that provides the best-fit χ^2, this reinforces the idea that the data prefers a model with a low amplitude of the pressure profile at small scales.

We then repeat the analysis using the Mead model for the lensing signal, instead of using the re-scaled NFW profiles. This approach is more conservative, as we let the data re-scale the lensing profile instead of relying on the power spectra measured on simulations. This approach is, however, less constraining, as we marginalise over the Mead model parameters using wide priors. In this case all the models provide a similar best fit χ^2. The fact that the best fit of all the different feedback models are similar is related to the large, uninformative prior on the Mead model parameters, which, together with the freedom allowed by the priors on the cosmological and nuisance parameters, absorbs most of the differences between models. Interestingly, the best fit χ^2 of all the models obtained freeing Mead model parameters is not too different from the best fit χ^2 obtained for the AGN 8.5 model and re-scaling the NFW profile.

We show in Fig. 11 the posterior of the Mead model parameters for each feedback models. In general, the feedback models prefer smaller A_{Mead} and larger η_{Mead} than the NFW profile (except for the A_{Mead} parameter for the AGN 8.5 feedback model), which implies less concentrated and more "bloated" halos. Lastly, we note that the UDM statistics for this second analysis is not in tension with the *Planck* prior (Fig. 10 and Table V), owing to a larger prior space.

We test whether our findings are robust against the exact value of the parameter β used to de-project the CIB contribution in the *Planck* map. To test this, we ran a full analysis using the measurements without CIB de-projection for
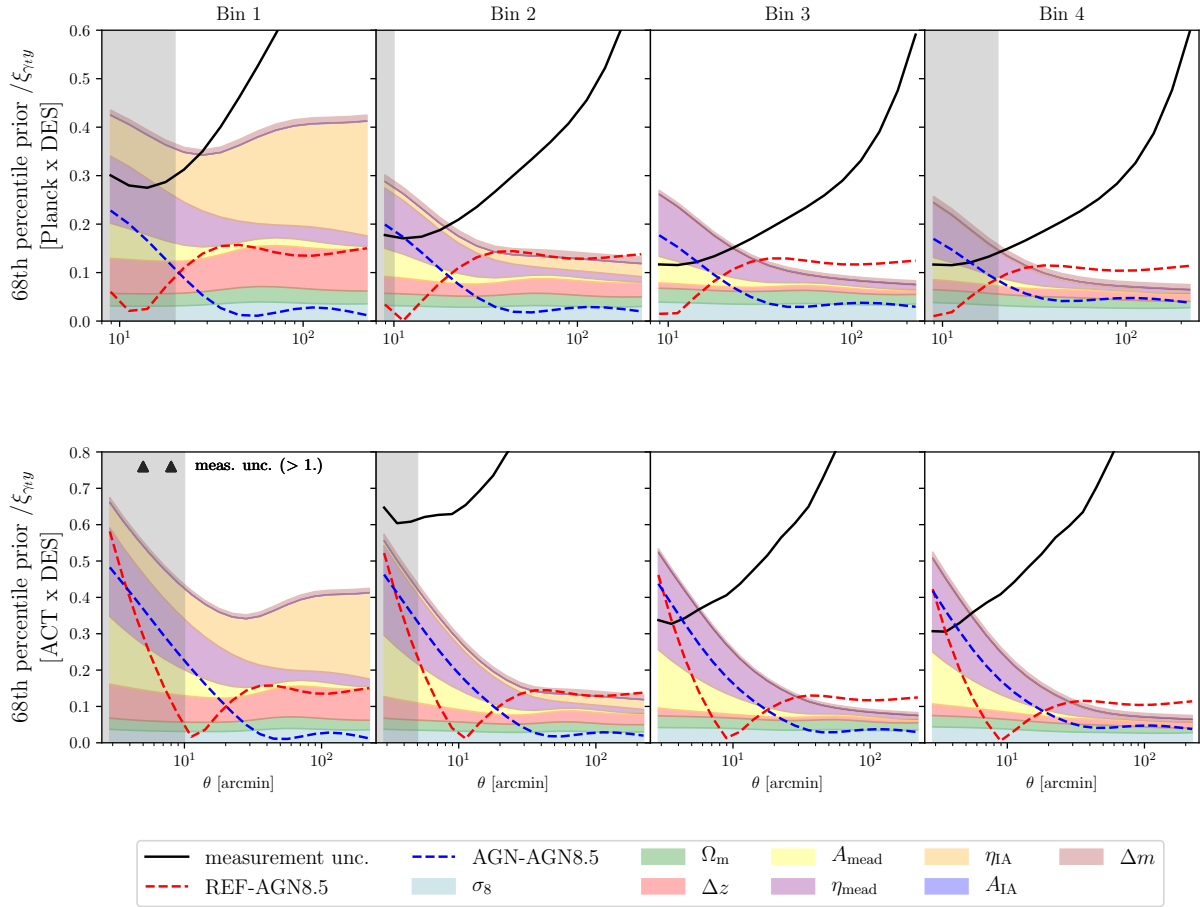
Figure 12. The plot assesses how our ability to discriminate among different feedback models is limited by our measurement uncertainties and nuisance parameters. In particular, the coloured bands show the contribution of each single nuisance parameter to the total 68% confidence interval of our prior. We assume *Planck* priors for σ_8 and Ω_m. The black line represents the measurement uncertainty. The vertical grey line indicates the scale cut adopted in this analysis (Table II). Quantities in the figure are divided by a theory data vector $\xi^{\gamma y}$ obtained for the AGN8.5 feedback model. We also show the fractional difference with respect to two other models: REF and AGN. Areas where the black line is below the combined prior budget can be used to differentiate between models.

the *Planck* x DES measurement. This is an extreme case, as we believe the CIB de-projection is necessary, and the value $\beta = 1.2$ used in the fiducial analysis is justified by [48]. Nonetheless, we confirm that also in this unrealistic case, when running using the re-scaled NFW profiles the data prefers the AGN 8.5 model in terms of best fit χ^2. We find, however, that the UDM tension metric increases for all the models[9]: neglecting the CIB de-projection makes our analysis prefer a different cosmology than *Planck*, but it does not have an impact on the feedback model selection.

Finally, we investigate the limitation in our ability to constrain different feedback models due to our measurement uncertainties and lack of tight priors on our nuisance parameters. This is shown in Fig. 12. The coloured bands show

the contribution of each single nuisance parameter to the total 68% confidence interval of our prior. Note that we assumed the *Planck* prior for σ_8 and Ω_m, and we considered the conservative scenario where we also marginalise over Mead model parameters. Quantities in Fig. 12 are shown with respect to a theory data vector obtained assuming the AGN8.5 model. We also show in the plot the fractional difference (in absolute value) with respect to two other feedback models (AGN, REF).

For the purposes of feedback model selection, the ideal situation would be a regime where differences between models are larger than measurement uncertainties (black lines), and that measurement uncertainties are not sub dominant with respect to the prior. This is not happening with our current data: our measurement uncertainties are generally larger than the difference between the models, except for a small window at $\sim 10-20$ arcmin in bin 3 and 4 for the *Planck* x DES measurement and small scales (< 5 arcmin) in bin 3 and 4 for the ACT x DES measurement. In this respect, future releases of the ACT Compton-*y* map [57] will definitely improve the situation. The next ACT Compton-*y* map will cover the full DES

---

[9] In particular, when assuming NFW re-scaling we obtain an UDM tension of 6.3σ, 3.8σ, 5.2σ, 6.1σ for the AGN, AGN 8.5, REF and TNG models, respectively. The UDM tension increases also when the Mead model is assumed: 2.3σ, 2.6σ, 1.2σ, 1.4σ, 2.0σ for the AGN, AGN 8.5, REF, TNG and B12 models, respectively.

Y3 footprint. This means that our measurement uncertainties from the ACT x DES correlations will be significantly smaller compared to the ones shown in this paper - as a comparison, they should be smaller than the ones quoted for *Planck* x DES in Fig. 12 (as in this work we removed a part of the *Planck* data), with the measurement extending down to small scales (∼ 2.5 arcmin).

In Fig. 12 we note the large contribution of the Mead model nuisance parameters to the 68% confidence interval of the prior. This is a substantial contribution that dominates the prior at scales < 20 arcminutes, and it explains why when marginalising over Mead model parameters our data could not discriminate among feedback models. At low redshift, uncertainties in the redshift estimates and intrinsic alignment parameter $\eta_{\rm IA}$ are also providing a substantial contribution (note that $A_{\rm IA}$ is instead tightly constrained by the prior, so it has a negligible impact and its 68% confidence interval cannot be seen in Fig. 12). This is expected as the lensing signal is smaller in amplitude at low redshift compared to higher redshift, and uncertainties on intrinsic alignment or redshift estimates can have a larger impact. When marginalising over the Mead model parameters, we did not assume any tight prior. In principle, one could estimate the correct values of $A_{\rm Mead}$ and $\eta_{\rm Mead}$ measuring the matter profiles in hydrodynamical simulations for the range of halo masses our measurement is sensitive to (which should be more accurate than just re-scaling the NFW profiles). Additional constraints on the Mead model parameters can be provided by a joint analysis with cosmic shear, including small scales (although cosmic shear is sensitive to lower mass halos compared to $\xi^{\gamma_t y}$). When varying Mead model parameters, we are not assuming any prior on the relation with the pressure profiles parameters; in principle, however, the two might be related. As we mentioned in § III B, since our Mead model is an effective model, it is hard to place physically motivated priors on the relation between the pressure profile parameters and the Mead model parameters. A joint cosmic shear and tSZ-shear analysis would benefit from having physically motivated priors relating the two sets of parameters, as this would help tighten the constraints. In this respect, more coherent frameworks (as the one introduced in Mead et al. [54]) where the shear and tSZ signals are modelled starting from the distribution of gas, matter, and stars, might be better suited to this task. Future analysis should also improve the modelling of intrinsic alignment; in this work we took a conservative approach and we removed a good portion of angular scales from the two lowest redshift bins due to the uncertainties in the modelling of the 1-halo IA contribution due to satellite galaxies alignment. A joint analysis with cosmic shear, with better IA modelling on small scales, could allow us to also use the smallest scales of our measurements at low redshift, with tighter constraints on IA nuisance parameters.

V. SUMMARY

This is the first of two works on cross-correlations between thermal Sunyaev-Zeldovich (tSZ) maps from *Planck* and the Atacama Cosmology Telescope (ACT) and weak gravitational lensing shears measured during the first three years of observations of the Dark Energy Survey (DES). This correlation is sensitive to the thermal energy in baryons as a function of redshift, and is in principle a powerful probe of astrophysical feedback. In this work we presented the cross-correlation measurements: we detected the correlation at a significance of 21σ, the highest significance to date. We also presented a series of systematic tests, where we tested the effect of potential contaminants on our measurements, including cosmic infrared background (CIB) and radio sources. We found that CIB has a substantial effect on the *Planck* x DES measurement, whereas the ACT x DES measurement was not significantly affected, probably due to the ACT Compton-*y* map receiving significant contributions from the ACT 98 and 150 GHz channels, where the CIB is relatively faint, and also due to the noisier nature of the latter measurement. In order to account for the CIB effect, we built a CIB de-projected Compton-*y* map for the *Planck* data and used it in our main analysis.

We then used the shear-*y* correlation measurements to test a number of different feedback models, modelling the correlations using the halo model formalism. In particular, we modelled the tSZ part of the signal using a number of different pressure profiles calibrated against hydrodynamical simulation which have implemented different baryonic feedback models. On the other hand, the shear part was modelled either using a re-scaled NFW profile or implementing the Mead halo model [53]. In the first approach, the NFW profile was re-scaled by a mass-independent factor given by the ratio of the power spectrum from a dark-matter only simulation and the power spectrum from a hydrodynamical simulation with dark-matter and a sub-grid prescription for baryonic effects. In the second approach, the lensing kernel was modelled by a generalised NFW profile [53] with extra degrees of freedom to take into account the effect of baryonic feedback processes. When comparing our models to our measurement, we kept the pressure profile model fixed, as our goal was to discriminate among different feedback models. Note that a different approach where the pressure profile parameters are varied is adopted in paper II.

In our analysis, we marginalised over 10 nuisance parameters capturing redshift uncertainties, shear calibration biases, and intrinsic alignment effects adopting DES priors. We also marginalised over $\Omega_{\rm m}$ and σ_8 using *Planck* and DES priors, and when used, over the Mead halo model parameters. We found when using the re-scaled NFW profile in combination with the pressure profiles from hydrodynamical simulations, the data preferred a lower amplitude of the pressure profile at small scales, compatible with a scenario with stronger AGN feedback and ejection of gas from the inner part of the halos (the AGN 8.5 model). We quantified the level of agreement/disagreement of each model with the data using Gaussian estimators [71], and we found that, when assuming *Planck* priors on the cosmological parameters $\Omega_{\rm m}$ and σ_8, all the models were in $3 - 4\sigma$ tension with the prior, except for the AGN 8.5 model, which showed a lower tension (2.2σ). This means that for a *Planck* cosmological model, the tSZ signal that we measure is in tension with the predictions of most of these feedback models (except for the AGN 8.5

model). When using the Mead model in combination with the pressure profiles from hydrodynamical simulations, we obtained weaker constraints due to the extra nuisance parameters of the model, for which we did not assume any tight prior. In this case, the data could not discriminate between different baryonic prescriptions, but generally preferred halos less concentrated and more bloated compared to a NFW profile.

We then discussed whether the lack of tight priors on the nuisance parameters is limiting our analysis, finding that the Mead model parameters are dominating our prior volume. We discussed how one could place tighter constraints on the Mead model parameters measuring the matter profiles in hydrodynamical simulations for the range of halo masses to which our measurement is sensitive. Additional constraints on the Mead model parameters could also be provided by a joint analysis with cosmic shear, including small scales - possibly with a more coherent, physically motivated framework, as the one introduced in Mead et al. [54]. In general, it might also be useful to include in future analyses additional correlations sensitive to different halo masses (e.g., Compton-y - galaxy cross-correlations or Compton-y auto-correlations), in order to be able to study feedback mechanisms over a wide range of halo masses. Last, we mentioned how future data and in particular future releases of the ACT Compton-y map (which will cover the full DES footprint) will improve our ability to discriminate between different feedback models, as these maps will allow us to measure with high accuracy the Compton-y shear correlation at small scales, where feedback models show a large variance. This will constitute a substantial improvement over current ACT data (which have a limited overlap with DES data and hence noisier cross-correlation measurements) and over *Planck* data, which have a low angular resolution that does not allow us to efficiently probe the small scale regime.

DATA AVAILABILITY

The full METACALIBRATION catalogue will be made publicly available following publication, at the URL https://des.ncsa.illinois.edu/releases. The code used to perform the tests in this manuscript will be made available upon reasonable request to the authors.

ACKNOWLEDGEMENTS

Appendix A: Validation on N-body simulations

We provide in this section further validation of our modelling by measuring the shear-Compton-y map cross correlation on the fiducial DES Y3 N-body simulations. Note that an independent modelling check on hydrodynamical simulations has been performed by [5], validating the use of the halo framework to model shear-Compton-y cross-correlations.

For this test, we use one realisation of the DES Y3 Buzzard catalogue v2.0 [14, 15]. Cosmological parameters of the simulation has been chosen to be $\Omega_m = 0.286$, $\sigma_8 = 0.82$, $\Omega_b = 0.047$, $n_s = 0.96$, $h = 0.7$. The lightcone of the simulation is generated on the fly starting from three boxes with different resolutions and sizes (1050^3, 2600^3 and 4000^3 Mpc$^3h^{-3}$ boxes and 1400^3, 2048^3 and 2048^3 particles); halos are identified using the public code ROCKSTAR [7] and they are populated with galaxies using ADDGALS [14]. Lensing effects are calculated using the multiple plane ray-tracing algorithm CALCLENS [6]. From the halo catalog, we construct a tSZ map by pasting a [4] profile on each halo. The map comes with in the `healpy` format with a resolution of `NSIDE` 4096. For this test, we do not smooth the map nor add instrumental noise. As for the simulated shape catalog, we use for this test a shape noise-free catalog, which faithfully reproduces DES Y3 area coverage and number density. Galaxies are further divided into four tomographic bins following the same methodology used on data.

We measure $\xi^{\gamma_t y}$ using the unsmoothed, noise-free simulated Compton-y map over the *Planck* footprint and the shape noise-free simulated shear catalog. As Buzzard is a DM-only N-body simulation, we model the signal using a NFW profile for the Fourier transform of the DM profile, rather than the Mead model. The comparison between the theory predictions and our measurements in simulations is shown in Fig. 13. We only show the result of this comparison for scales larger than 20 arcminutes. Below such a scale, the simulation becomes unreliable, as the measurement points receive significant contributions from scales below the simulation resolution ($k = 3h/$Mpc). In the scales where the comparison can be trusted, there is a very good match between the measurement and the theoretical predictions (the slight offest at large scales for bin 3 and 4 is compatible with cosmic variance, which is captured by the error bars). In particular, for the four tomographic bins, we obtain a $\chi^2 = 3, 4, 4, 5$ for 9 *d.o.f.*.

As a final test, we fitted our measurements using the Mead model, rather than the NFW profile, fixing all the parameters of our modelling except for the two Mead model parameters, which were sampled using broad flat priors. The Mead model encompasses the NFW profile as a subset of its parameter space, but it has additional flexibility. Indeed, the Mead model can provide a god fit for the Buzzard measurement at all scales.

Appendix B: Covariance Validation

We model the covariance $\mathbb{C}$ of the convergence and Compton-y cross-spectra as a sum of Gaussian ($\mathbb{C}^G$) and non-Gaussian ($\mathbb{C}^{NG}$) terms as follows:

$$\mathbb{C}(C_{\ell_1}^{\kappa,y_i}, C_{\ell_2}^{\kappa,y_j}) = \mathbb{C}^G(C_{\ell_1}^{\kappa,y_i}, C_{\ell_2}^{\kappa,y_j}) + \mathbb{C}^{NG}(C_{\ell_1}^{\kappa,y_i}, C_{\ell_2}^{\kappa,y_j}), \quad \text{(B1)}$$

where κ refers to the DES convergence field and y_i, y_j represent either the *Planck* or ACT Compton-y field. The Gaussian term is given by [31]:

$$\mathbb{C}^G(C_{\ell_1}^{\kappa,y_i}, C_{\ell_2}^{\kappa,y_i}) = \frac{\delta_{\ell_1\ell_2}}{f_{\text{sky}}^{\kappa,y_i;\kappa,y_j}(2\ell_1 + 1)\Delta\ell_1}\Big[\hat{C}_{\ell_1}^{\kappa,\kappa}\hat{C}_{\ell_2}^{y_i,y_j} + \hat{C}_{\ell_1}^{\kappa,y_j}\hat{C}_{\ell_2}^{\kappa,y_i}\Big].$$
$$\text{(B2)}$$

Here, $\delta_{\ell_1\ell_2}$ is the Kronecker delta, $f_{\text{sky}}^{\kappa,y_i;\kappa,y_j}$ is the effective sky coverage fraction, $\Delta\ell_1$ is the size of the multipole bin, and $\hat{C}_\ell$ is the total cross-spectrum between any pair of fields including the noise contribution. The non-Gaussian part, can be written following [49]:

$$\mathbb{C}^{NG}(C_{\ell_1}^{\kappa,y_i}, C_{\ell_2}^{\kappa,y_j}) = \frac{1}{4\pi f_{\text{sky}}^{\kappa,y_i;\kappa,y_j}}T_{\ell_1\ell_2}^{\kappa,y_i\kappa,y_j}, \quad \text{(B3)}$$

with

$$T_{\ell_1\ell_2}^{\kappa,y_i\kappa,y_j} = \int dz\frac{dV}{dzd\Omega}\int dM\frac{dn}{dM}\bar{\kappa}_{\ell_1}\bar{y}_{i,\ell_1}\bar{\kappa}_{\ell_2}\bar{y}_{j,\ell_2}. \quad \text{(B4)}$$

The real-space covariance for the measurement is then obtained by:

$$\mathbb{C}(\xi^{\gamma_t y_i}(\theta_1), \xi^{\gamma_t y_j}(\theta_2)) = \int \frac{d\ell_1\,\ell_1}{2\pi}J_2(\ell_1\theta_1)\times$$
$$\int \frac{d\ell_2\,\ell_2}{2\pi}J_2(\ell_2\theta_2)\mathbb{C}(C_{\ell_1}^{\kappa,y_i}, C_{\ell_2}^{\kappa,y_j}). \quad \text{(B5)}$$

In order to validate the covariance matrix, we follow [49] and perform a comparison with a covariance matrix estimated through jackknife resampling of the measurement on data. In particular, we use the following expression [59]:

$$\hat{\Sigma}(x_i, x_j) = \frac{(N_{JK} - 1)}{N_{JK}}\sum_{k=1}^{N_{JK}}(x_i^k - \bar{x}_i)(x_j^k - \bar{x}_j), \quad \text{(B6)}$$

where the sample is divided into $N_{JK} = 200$ sub-regions of roughly equal area, x_i is a measure of the statistic of interest in the i-th bin of the k-th sample, and $\bar{x}_i$ is the mean of our resamplings. Note that the jackknife resampling only allows to efficiently estimate the covariance matrix on scales
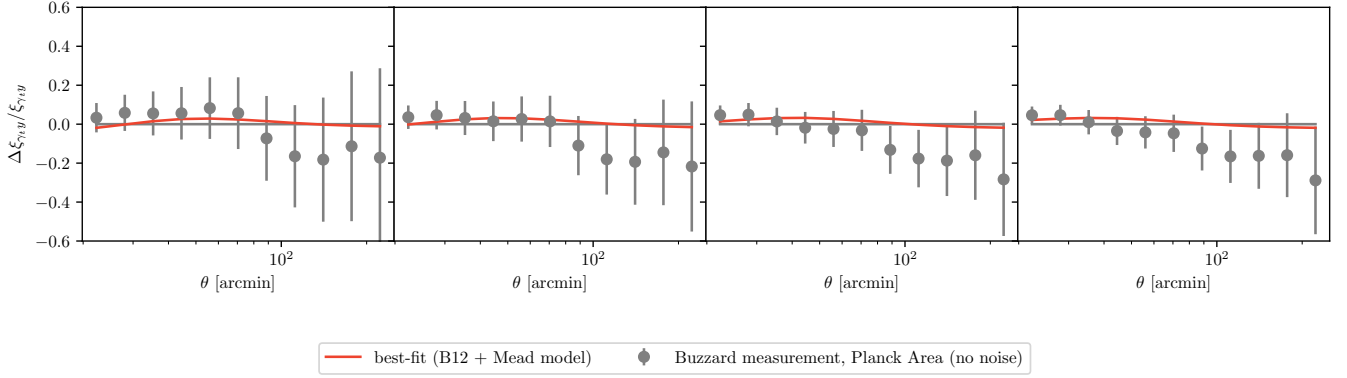
Figure 13. Comparison between the measured $\xi^{\gamma_t y}$ in Buzzard simulation and our theory predictions. In particular, we report the fractional difference with respect to the theory predictions. Theory predictions have been obtained assuming a B12 pressure profile and NFW profile for the DM profile. Grey points represent the measurement on a unsmoothed, noise-free realisation of Buzzard. Uncertainties are estimated using a noise-free theoretical covariance. Measurement points are very correlated (both among different redshift bins and angular scales). The red line represents the best fit to the data performed using the Mead model instead of the NFW profile.
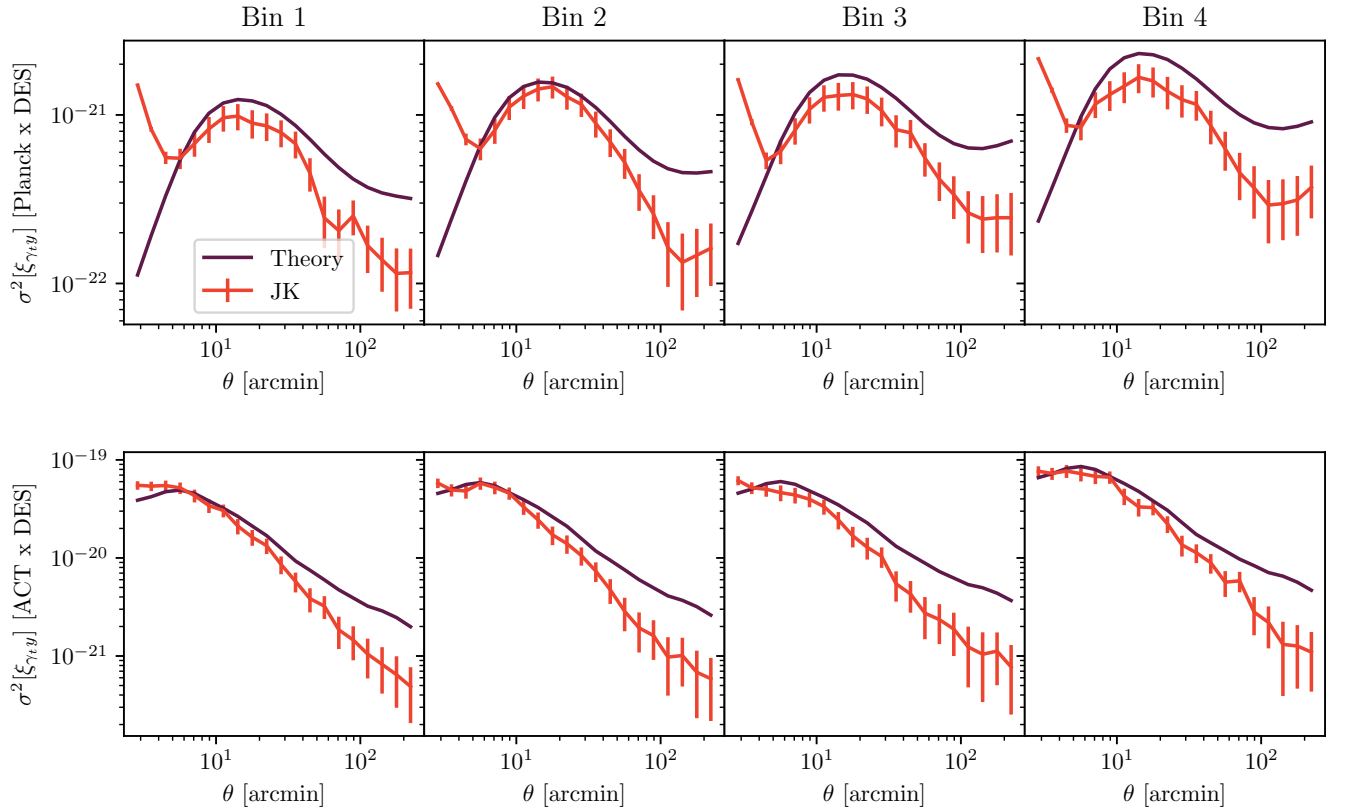

Figure 14. Diagonal elements of the covariance matrix, for the *Planck* and DES $\xi^{\gamma_t y}(\theta)$ (top panels) and ACT and DES $\xi^{\gamma_t y}(\theta)$ (lower panels), for the four different DES tomographic bins. In each panel, we compare theory predictions (purple) to jackknife estimates (JK, red).

smaller than the size of the jackknife patches, so the jackknife covariance will be biased low at large scales. The comparison between the theoretical and the jacckknife covariance for the $\xi^{\gamma_t y}$ measurements is shown in Fig. 14, and shows good agreement at small-intermediate scales, where the jackknife covariance can be considered reliable. Note that the range of scales where this comparison holds is smaller for ACT, since

average size of the JK patch is much smaller than in the case of *Planck*. In the case of *Planck*xDES covariance, the jackknife estimates have an upturn for scales smaller than 5 arcminutes which is not captured by our analytical covariance. Our guess is that this is related to mask effects; however, we did not investigate this further, as in the case of *Planck*xDES measurement we exclude scales < 8 arcminutes due to *Planck*
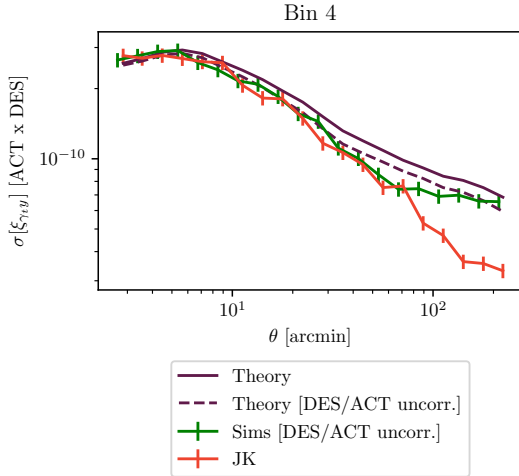
Figure 15. Diagonal elements of the covariance matrix, for the fourth tomographic bin, for the ACTxDES $\xi^{\gamma_t y}(\theta)$. In addition to theory predictions (purple) and jackknife estimates (JK, red), we also show the estimates obtained by using ACT simulations and DES data (green), and the theory predictions that neglect correlations between ACT and DES (purple, dashed lines).

beam FWHM.

The $\xi^{\gamma_t y}$ measurement involving DES and ACT map is also validated cross-correlating 300 simulated ACT maps with the DES Y3 shape catalog. These measurements should capture the dominant part of the Gaussian part of the covariance ($\propto \hat{C}_{\ell_1}^{\kappa,\kappa} \hat{C}_{\ell_2}^{y_i,y_j}$), but they cannot capture the terms $\hat{C}_{\ell_1}^{\kappa,y_j} \hat{C}_{\ell_2}^{\kappa,y_i}$ and the non gaussian part of the covariance, since the large-scale fluctuations of the simulated Compton y-maps are not correlated with the data one from the shear catalog. This is still a relevant comparison as these two latter terms should not dominate in the case of the ACTxDES measurement.

However, the non Gaussian part of the covariance is expected to be sub-dominant when cross correlating ACT with DES, so this should not strongly affect the comparison. Fig. 15 shows the diagonal elements of the covariance matrix estimated using ACT simulations, showing a better match with theory at large scales compared to jackknife estimates. For comparison purposes, we also show the theory covariance matrix computed dropping terms that are not captured by the measurement in simulations.

Appendix C: Tests on Websky mocks on CIB contamination

We further discuss in the Appendix the impact that the CIB can have on our measurements when the Compton-y maps are not generated by explicitly de-projecting the CIB signal. In our analysis, this has proven to be necessary for the *Planck* x DES measurement, whereas we found no significant CIB contamination of the ACT x DES signal, owing to the lower signal-to-noise of the latter. To this aim, we use Websky mocks [82], which are full-sky simulations of the extragalactic microwave sky generated using the mass-Peak Patch approach. We use Compton-y, lensed CMB and CIB maps for frequencies 143, 217, 353, and 545 GHz, convolved with the
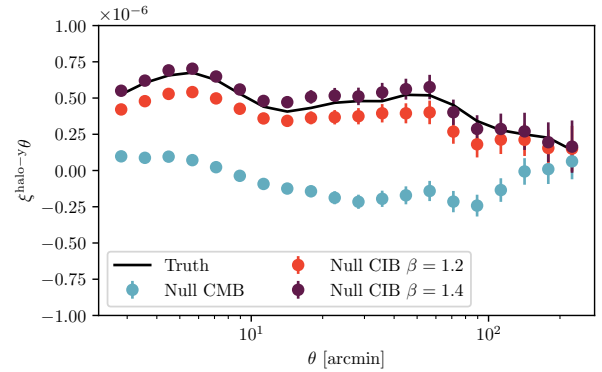

Figure 16. Halo-Compton-y correlation from Websky mocks. The three different measurements use three different versions of the Compton-y maps. The black line refers to the case where the Compton-y map is created starting from frequency channels without CIB contamination, whereas the two other measurements have been obtained using frequency channels contaminated by a fiducial CIB signal, with or without CIB de-projection at the map-making level.

nominal *Planck* Gaussian beam and with *Planck*-like white noise [66]. We created two sets of maps for each frequency channel: one with CIB contamination, and one without CIB contamination. Last, we created three Compton-y maps using our NILC algorithm: a first map from the frequency channels without CIB contamination, a second map from the frequency channels with CIB contamination but without explicitly de-projecting the CIB signal, and a third one using the CIB contaminated frequency maps and de-projecting the CIB signal during the map making process. When de-projecting the CIB signal, we used $\beta = 1.2$. The Websky mocks do not have shear maps available, but they provide a dark matter halo catalog. To qualitatively span the same redshift and halo mass range probed by our measurement, we selected halos so as to have a sample with average mean redshift $\langle z \rangle \sim 0.25$ and average halo mass $10^{14.3} M_\odot$. This corresponds to the typical redshift and halo mass of our measurement involving the 4th tomographic bin (see paper II). We then computed the halo Compton-y correlation signal (obtained cross correlating the halos positions with the values of the Compton-y maps). We show in Fig. 16 the measurements with the three different Compton-y maps. The angular scale sensitivity of this halo-Compton-y correlation is expected to be different from the shear-Compton-y correlation; moreover, when creating the simulated Compton-y maps we did not use any frequency channels below 143 GHz, contrary to the maps on data. For these reasons, the effect of CIB on these measurements cannot be directly compared to the effect of CIB we see on data. Nonetheless, from Fig. 16 is clear that if no CIB de-projection is implemented when making the Compton-y map, the resulting measurement can be strongly biased.

Appendix D: Tests of feedback models using DES prior

We show in this Appendix the constraints of feedback models obtained using DES priors on σ_8 and Ω_m. Table VI shows

Table VI. Best fit χ^2 for the four feedback models (B12, AGN, AGN8.5, REF), obtained assuming *Planck* on σ_8 and Ω_m, and marginalising over nuisance parameters as explained in § III D. The top table refers to the models obtained re-scaling the NFW profile for the lensing signal; on the other hand, the bottom table refers to the analysis where we model the lensing signal using the Mead model. We also report the update-difference-in-mean (UDM) tension for the best fit models with respect to their priors.

DES prior (NFW re-scaling)					
	B12	**AGN**	**AGN 8.5**	**REF**	**TNG**
$\chi^2/d.o.f.$	-	170/119	158/119	187/119	194/119
UDM tension	-	$0.5\,\sigma$	$0.1\,\sigma$	$0.3\,\sigma$	$0.6\,\sigma$
DES prior (free A_{Mead},η_{Mead})					
	B12	**AGN**	**AGN 8.5**	**REF**	**TNG**
$\chi^2/d.o.f.$	154/118	154/118	154/118	156/118	154/118
UDM tension	$0.7\,\sigma$	$0.2\,\sigma$	$0.3\,\sigma$	$0.2\,\sigma$	$053\,\sigma$

the best-fit χ^2 and the update-difference-in-mean (UDM) tension for the different feedback scenarios, for both cases where we use the NFW re-scaling to model the lensing part of our signal and where we use the Mead model instead. The posteriors of σ_8 and Ω_m are shown in Fig. 17. The main difference with respect to our analysis using *Planck* prior (§ IV D) concerns the UDM tension metric, which does not show any sign of tension with the DES prior owing to the broader prior from the DES analysis compared to *Planck*. Besides this, similar to the *Planck* prior case, we find that when implementing the NFW re-scaling, the data prefers the AGN 8.5 scenarios, whereas when implementing the Mead model, we are not able to discriminate among different feedback scenarios, owing to the less constraining nature of this modelling choice.

[1] Abbott, T. M. C., Abdalla, F. B., Alarcon, A., et al., 2018, Phys. Rev. D, 98, 4, 043526
[2] Aihara, H., Armstrong, R., Bickerton, S., et al., 2018, PASJ, 70, S8
[3] Asgari, M., Lin, C.-A., Joachimi, B., et al., 2021, A&A, 645, A104
[4] Battaglia, N., Bond, J. R., Pfrommer, C., Sievers, J. L., 2012, The Astrophysical Journal, 758, 2, 75, ISSN 1538-4357
[5] Battaglia, N., Hill, J. C., Murray, N., 2015, ApJ, 812, 2, 154
[6] Becker, M. R., 2013, MNRAS, 435, 115
[7] Behroozi, P. S., Wechsler, R. H., Wu, H.-Y., 2013, ApJ, 762, 109
[8] Bridle, S., King, L., 2007, New Journal of Physics, 9, 444
[9] Chiang, Y.-K., Makiya, R., Ménard, B., Komatsu, E., 2020, ApJ, 902, 1, 56
[10] Chisari, N. E., Mead, A. J., Joudaki, S., et al., 2019, The Open Journal of Astrophysics, 2, 1, 4
[11] Cooray, A., Sheth, R., 2002, Phys. Rep., 372, 1, 1
[12] Cordero, J. P., Harrison, I., et al., 2020, To be submitted to MNRAS
[13] Delabrouille, J., Cardoso, J. F., 2009, Diffuse Source Separation in CMB Observations, vol. 665, 159–205
[14] DeRose, J., Wechsler, R. H., Becker, M. R., et al., 2019, arXiv e-prints, arXiv:1901.02401
[15] DeRose, J., Wechsler, R. H., Becker, M. R., et al., 2021, arXiv e-prints, arXiv:2105.13547
[16] Eifler, T., Krause, E., Dodelson, S., Zentner, A. R., Hearin, A. P., Gnedin, N. Y., 2015, MNRAS, 454, 3, 2451
[17] Flaugher, B., Diehl, H. T., Honscheid, K., et al., 2015, AJ, 150, 150
[18] Fortuna, M. C., Hoekstra, H., Joachimi, B., et al., 2021, MNRAS, 501, 2, 2983
[19] Gatti, M., Sheldon, E., Amon, A., et al., 2021, MNRAS, 504, 3, 4312
[20] Guilloux, F., Fay, G., Cardoso, J.-F., 2007, arXiv e-prints, arXiv:0706.2598
[21] Handley, W. J., Hobson, M. P., Lasenby, A. N., 2015, MNRAS, 450, L61
[22] Handley, W. J., Hobson, M. P., Lasenby, A. N., 2015, MNRAS, 453, 4, 4384
[23] Hartley, W. G., Choi, A., et al., 2020, To be submitted to MNRAS
[24] Hellwing, W. A., Schaller, M., Frenk, C. S., et al., 2016, MNRAS, 461, L11
[25] Hikage, C., Oguri, M., Hamana, T., et al., 2019, PASJ, 71, 2, 43
[26] Hildebrandt, H., Viola, M., Heymans, C., et al., 2017, MNRAS, 465, 2, 1454
[27] Hill, J. C., Pajer, E., 2013, Phys. Rev. D, 88, 6, 063526
[28] Hill, J. C., Spergel, D. N., 2014, JCAP, 2014, 2, 030
[29] Hirata, C. M., Seljak, U., 2004, Phys. Rev. D, 70, 6, 063526
[30] Hojjati, A., Tröster, T., Harnois-Déraps, J., et al., 2017, MNRAS, 471, 2, 1565
[31] Hu, W., Jain, B., 2004, Phys. Rev. D, 70, 4, 043009
[32] Huang, H.-J., Eifler, T., Mandelbaum, R., Dodelson, S., 2019, MNRAS, 488, 2, 1652
[33] Huang, H.-J., Eifler, T., Mandelbaum, R., et al., 2021, MNRAS, 502, 4, 6010
[34] Huff, E., Mandelbaum, R., 2017, arXiv e-prints, 1702.02600
[35] Huffenberger, K., et al., 2020, in preparation
[36] Jarvis, M., Bernstein, G., Jain, B., 2004, MNRAS, 352, 1, 338
[37] Joudaki, S., Blake, C., Heymans, C., et al., 2017, MNRAS, 465, 2, 2033
[38] Komatsu, E., Kitayama, T., 1999, ApJ, 526, 1, L1
[39] Komatsu, E., Seljak, U., 2002, MNRAS, 336, 4, 1256
[40] Krause, E., Eifler, T. F., Zuntz, J., et al., 2017, arXiv e-prints, arXiv:1706.09359
[41] Kuijken, K., Heymans, C., Hildebrandt, H., et al., 2015, MNRAS, 454, 4, 3500
[42] Laureijs, R., Amiaux, J., Arduini, S., et al., 2011, arXiv e-prints, arXiv:1110.3193
[43] Le Brun, A. M. C., McCarthy, I. G., Melin, J.-B., 2015, Monthly Notices of the Royal Astronomical Society, 451, 4, 3868
[44] Le Brun, A. M. C., McCarthy, I. G., Schaye, J., Ponman, T. J., 2014, MNRAS, 441, 2, 1270
[45] LSST Science Collaboration, Abell, P. A., Allison, J., et al., 2009, arXiv e-prints, arXiv:0912.0201
[46] MacCrann, N., Aleksić, J., Amara, A., et al., 2017, MNRAS, 465, 3, 2567
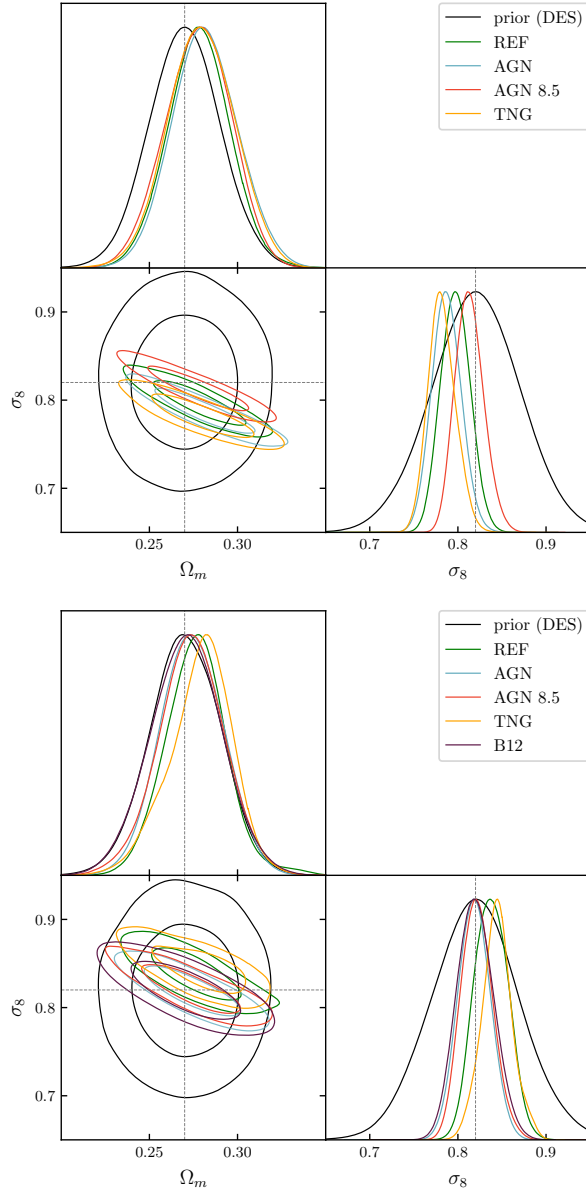
Figure 17. Posterior for the parameters σ_8 and Ω_m for the four (five) feedback models: (B12), REF, AGN, AGN 8.5 and TNG. We also show the *DES* prior. Top refers to the case where we used the NFW re-scaling to model the lensing part of our signal; the bottom plot refers to the more conservative analysis where we used the Mead model.

[47] MacCrann, N., Becker, M. R., McCullough, J., et al., 2020, arXiv e-prints, arXiv:2012.08567

[48] Madhavacheril, M. S., Hill, J. C., Næss, S., et al., 2020, Phys. Rev. D, 102, 2, 023534

[49] Makiya, R., Ando, S., Komatsu, E., 2018, MNRAS, 480, 3, 3928

[50] McCarthy, I. G., Schaye, J., Bird, S., Le Brun, A. M. C., 2017, MNRAS, 465, 3, 2936

[51] Mead, A. J., Brieden, S., Tröster, T., Heymans, C., 2021, MN-RAS, 502, 1, 1401

[52] Mead, A. J., Heymans, C., Lombriser, L., Peacock, J. A., Steele, O. I., Winther, H. A., 2016, MNRAS, 459, 2, 1468

[53] Mead, A. J., Peacock, J. A., Heymans, C., Joudaki, S., Heavens, A. F., 2015, MNRAS, 454, 2, 1958

[54] Mead, A. J., Tröster, T., Heymans, C., Van Waerbeke, L., Mc-Carthy, I. G., 2020, A&A, 641, A130

[55] Moser, E., Amodeo, S., Battaglia, N., Alvarez, M. A., Ferraro, S., Schaan, E., 2021, arXiv e-prints, arXiv:2103.02469

[56] Myles, J., Alarcon, A., Amon, A., et al., 2021, MNRAS, 505, 3, 4249

[57] Naess, S., Aiola, S., Austermann, J. E., et al., 2020, JCAP, 2020, 12, 046

[58] Navarro, J. F., Frenk, C. S., White, S. D. M., 1996, ApJ, 462, 563

[59] Norberg, P., Baugh, C. M., Gaztañaga, E., Croton, D. J., 2009, MNRAS, 396, 19

[60] Osato, K., Shirasaki, M., Miyatake, H., et al., 2020, MNRAS, 492, 4, 4780

[61] Pandey, S., Baxter, E. J., Xu, Z., et al., 2019, Phys. Rev. D, 100, 6, 063519

[62] Pandey, S., et al., 2021, in preparation

[63] Planck Collaboration, Ade, P. A. R., Aghanim, N., et al., 2014, A&A, 571, A28

[64] Planck Collaboration, Ade, P. A. R., Aghanim, N., et al., 2014, A&A, 571, A30

[65] Planck Collaboration, Ade, P. A. R., Aghanim, N., et al., 2016, A&A, 594, A2

[66] Planck Collaboration, Aghanim, N., Akrami, Y., et al., 2020, A&A, 641, A3

[67] Planck Collaboration, Aghanim, N., Akrami, Y., et al., 2020, A&A, 641, A6

[68] Planck Collaboration, Aghanim, N., Arnaud, M., et al., 2016, A&A, 594, A22

[69] Prat, J., Blazek, J., Sánchez, C., et al., 2021, arXiv e-prints, arXiv:2105.13541

[70] Quenouille, M. H., 1949, Proceedings of the Cambridge Philosophical Society, 45, 3, 483

[71] Raveri, M., Hu, W., 2019, Phys. Rev. D, 99, 4, 043506

[72] Remazeilles, M., Delabrouille, J., Cardoso, J.-F., 2011, MN-RAS, 418, 1, 467

[73] Samuroff, S., Blazek, J., Troxel, M. A., et al., 2019, MNRAS, 489, 4, 5453

[74] Schaan, E., Ferraro, S., Amodeo, S., et al., 2021, Phys. Rev. D, 103, 6, 063513

[75] Schmidt, S. J., Ménard, B., Scranton, R., Morrison, C. B., Rahman, M., Hopkins, A. M., 2015, MNRAS, 446, 3, 2696

[76] Semboloni, E., Hoekstra, H., Schaye, J., 2013, MNRAS, 434, 1, 148

[77] Sevilla-Noarbe, I., Bechtol, K., Carrasco Kind, M., et al., 2021, ApJS, 254, 2, 24

[78] Sheldon, E. S., Huff, E. M., 2017, ApJ, 841, 24

[79] Sheldon, E. S., Johnston, D. E., Frieman, J. A., et al., 2004, AJ, 127, 5, 2544

[80] Shirasaki, M., 2018, Monthly Notices of the Royal Astronomical Society, 483, 1, 342–351, ISSN 1365-2966

[81] Springel, V., Pakmor, R., Pillepich, A., et al., 2018, MNRAS, 475, 1, 676

[82] Stein, G., Alvarez, M. A., Bond, J. R., 2019, MNRAS, 483, 2, 2236

[83] Sunyaev, R. A., Zeldovich, I. B., 1980, ARA&A, 18, 537

[84] Sunyaev, R. A., Zeldovich, Y. B., 1972, Comments on Astrophysics and Space Physics, 4, 173

[85] Tinker, J., Kravtsov, A. V., Klypin, A., et al., 2008, ApJ, 688, 709

[86] Tinker, J. L., Robertson, B. E., Kravtsov, A. V., et al., 2010, ApJ, 724, 878

[87] Troxel, M. A., MacCrann, N., Zuntz, J., et al., 2018, Phys. Rev. D, 98, 4, 043528

[88] van Daalen, M. P., McCarthy, I. G., Schaye, J., 2020, MNRAS, 491, 2, 2424

[89] van Daalen, M. P., Schaye, J., Booth, C. M., Dalla Vecchia, C., 2011, MNRAS, 415, 4, 3649

[90] Van Waerbeke, L., Hinshaw, G., Murray, N., 2014, Phys. Rev. D, 89, 2, 023508

[91] Yan, Z., Hojjati, A., Tröster, T., Hinshaw, G., van Waerbeke, L., 2019, ApJ, 884, 2, 139